ACS APPLIED MATERIALS & INTERFACES

www.acsami.org

Research Article

Injectable Hydrogel for Cardiac Repair via Dual Inhibition of Ferroptosis and Oxidative Stress

Jiazhuo Gong, Yuwei Qiu, Chaojie Yu, Cheng Cao, Xiuqiang Li, Jiajun Lu, Weiqing Zhao, Zhongming Zhao, Haitao Zhang, Fanglian Yao, Hong Sun,* Hong Zhang,* and Junjie Li*

Cite This: *ACS Appl. Mater. Interfaces* 2025, 17, 27906−27922

Read Online

ACCESS | Metrics & More | Article Recommendations | Supporting Information

ABSTRACT: Ferroptosis plays a significant role in ischemic heart disease by exacerbating myocardial injury through oxidative stress, iron metabolism disorder, and inflammation. Herein, we develop an injectable hydrogel (HSD/DFO@GMs) with antiferroptosis and antioxidant properties for cardiac repair. The hydrogel is composed of dopamine-grafted oxidized hyaluronic acid, adipic acid dihydrazide grafted hyaluronic acid, and deferoxamine loaded gelatin microsphere, connected via a dynamic Schiff base bond. This hydrogel exhibits a favorable injectability and stable mechanical properties. It effectively chelates Fe^{2+} and scavenges the reactive oxygen species (ROS), creating a conducive microenvironment for cardiac repair. The dynamic Schiff base bond and gelatin matrix respond to the weakly acidic and MMP-2-rich microenvironment postinjury, enabling on-demand release of DFO in the injured myocardium. In vitro experiments indicate that the hydrogel significantly inhibits the ferroptosis and oxidative stress damage in H9C2 cardiomyocytes under a hypoxia/reoxygenation microenvironment. In an in vivo ischemia−reperfusion model, the HSD/DFO@GMs hydrogel reduces oxidative stress, modulates intracellular labile iron pool levels, and promotes revascularization, ultimately improving cardiac function. Overall, the HSD/DFO@GMs hydrogel provides a new strategy to improve cardiac repair by inhibiting ferroptosis and mitigating oxidative stress damage.

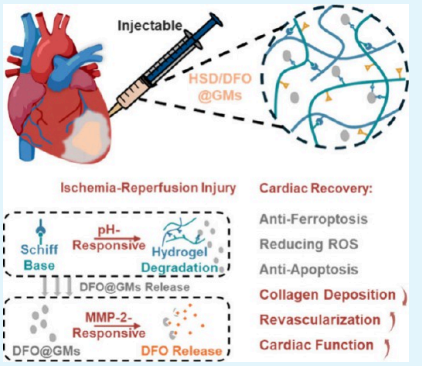

KEYWORDS: *ferroptosis, injectable hydrogels, iron ions chelating and ROS scavenging, responsive release, myocardial ischemia−reperfusion injury*

1. INTRODUCTION

Ischemic heart disease is recognized as the foremost global cause of mortality.[1] Ischemia−reperfusion injury (I/R) is a primary driver of cardiac damage.[2,3] I/R injury is characterized by the generation of substantial reactive oxygen species (ROS), leading to significant oxidative stress damage in cardiomyocytes. Moreover, it leads to multiple forms of programmed cell death, including apoptosis, pyroptosis, and ferroptosis,[4,5] which ultimately result in adverse outcomes such as malignant ventricular remodeling and heart failure. Among these, ferroptosis, an emerging paradigm of regulated cell death, is fundamentally an iron-dependent phenomenon catalyzed by lipid peroxidation. This distinctive form of cell demise is typified by the buildup of lipid peroxides and ROS.[6−8] Ferroptosis has garnered significant attention for its crucial role in the pathophysiology of I/R injury.[9,10] Therefore, there is a pressing need to develop biomaterials capable of inhibiting ferroptosis and mitigating oxidative stress damage, while ferroptosis has garnered significant interest in cancer therapy due to its potential for inducing tumor cell death.[11] However, the development of biomaterials, such as hydrogels, to inhibit ferroptosis in I/R-injured cardiac tissues is still in its infancy.[12] This gap in research highlights the need for further investigation into antiferroptosis biomaterials to enhance cardiac repair.

The occurrence of ferroptosis following I/R injury can be attributed to the dysregulation of cellular iron homeostasis and the failure of the defense mechanisms. The free iron content in the infarcted area is upregulated and subsequently endocytosed by cardiomyocytes for storage in a labile iron pool (LIP).[13,14] This process leads to the upregulation of iron-containing lipoxygenases and produces hydroxyl radicals (•OH) via the Fenton reaction, which in turn produces lipid peroxides (LPOs) and exacerbates ferroptosis.[15] Additionally, the overproduction of ROS in the I/R-injured area creates a vicious cycle involving inflammation and mitochondrial dysfunction.[16,17] Therefore, the concurrent removal of excess iron and ROS from the infarcted area is a crucial strategy to inhibit ferroptosis and oxidative stress damage, thereby attenuating I/R injury. Hydrogels possess the remarkable

Received: February 8, 2025
Revised: April 25, 2025
Accepted: April 26, 2025
Published: May 6, 2025

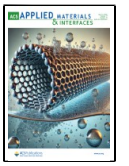

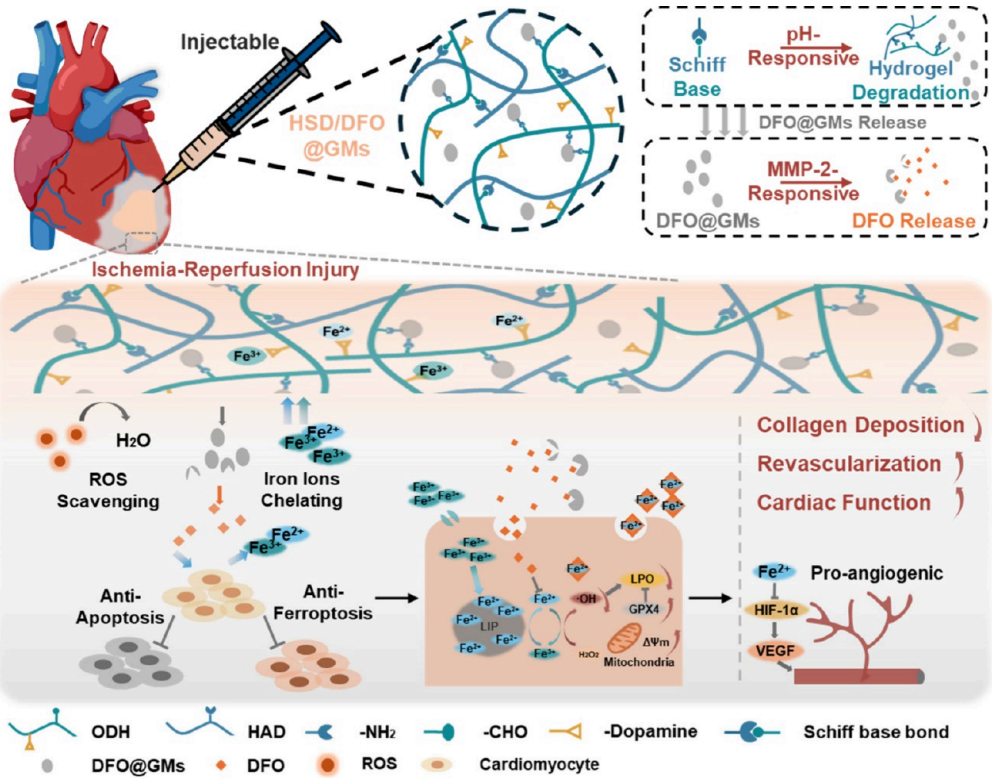

Figure 1. Schematic illustration of HSD/DFO@GMs hydrogel with antiferroptosis and antioxidant properties for treatments of myocardial I/R injury.

ability to effectively chelate iron ions through metal coordination interactions between their functional groups (such as carboxyl, hydroxyl, and amino groups) with Fe^{2+}/Fe^{3+} ions. Additionally, the chelation of iron ions can also be facilitated through dynamic covalent or noncovalent bonds with the hydrogel network, including hydrogen bonds and hydrophobic interactions. For example, Chekini et al. prepared a cellulose nanocrystals and gelatin-based hydrogel with a high absorption capacity for iron ions, which can act as an antibacterial wound dressing for repairing injured skin.[18] Chen et al. prepared a hydrogel using polyether F127 diacrylate and tannin, which is capable of adsorbing exogenous iron and remodeling the iron metabolism of cells.[19] Hyaluronic acid (HA) is a naturally occurring anionic polysaccharide that had been widely used in cardiac tissue engineering because it exhibits exceptional biocompatibility and minimal risk of triggering immune responses or tissue rejection.[20,21] Moreover, the large number of carboxyl groups in HA can chelate iron ions,[22] which provided the possibility to remodeling the ferroptosis process. However, it is difficult to modulate the ROS microenvironment, owing to low antioxidant activity. Dopamine (DA) molecules contain catechol groups and amino groups, which can react with free radicals to neutralize ROS and reduce oxidative stress.[23] Moreover, they can regulate intracellular iron metabolism by chelating iron ions and further suppress ferroptosis. For example, Zhang et al., suggested that the polydopamine nanoparticles can efficiently reduce Fe^{2+} accumulation, suppress LPO, and rejuvenate mitochondrial function in PC12 cells.[24] Therefore, the development of hydrogels based on HA and DA holds promise for regulating ferroptosis in I/R-injured myocardium.

To improve the effect of hydrogel on inhibiting ferroptosis, some ferroptosis inhibitors and iron chelators have the potential to be used to incorporated into the hydrogel network, such as ferrostatin-1, liproxstatin-1, adriamycin, vitamin A, and deferoxamine (DFO), etc.[14,25−27] Among them, the FDA-approved iron chelator DFO has been shown to reduce the risk of ferroptosis in the model of cardiac I/R injury.[28,29] In addition, DFO can inhibit prolyl hydroxylase by chelating intracellular Fe^{2+} to promote hypoxia-inducible factor 1α (HIF-1α) activity, which stimulates the activation of a range of pro-angiogenic genes including vascular endothelial growth factor (VEGF).[30,31] Currently, the treatment of various diseases caused by iron overload is often administered with DFO in high doses for long periods of time by means of subcutaneous injections.[32,33] Previous studies suggested that DFO demonstrates cytotoxicity toward human umbilical vein endothelial cells (HUVECs), macrophages, and other cells in a concentration-dependent manner.[34,35] Moreover, DFO faces challenges in effectively accumulating in the infarcted area and susceptibility to systemic toxicity.[36] Additionally, the application of DFO is severely limited by a very short half-life in plasma (20 min).[37] Consequently, the local delivery of DFO has emerged as a promising strategy to enhance therapeutic efficacy while minimizing systemic toxicity. Injectable hydrogels offer an effective approach to delivery of DFO directly to the I/R-injured area, enabling controlled release and thereby mitigating cytotoxicity that may arise from excessive local concentrations. Notably, the post-I/R cardiac microenvironment, characterized by its weakly acidity[38,39] and the presence of matrix metalloprotein protease-2 (MMP-2),[40,41] provides a unique opportunity to design DFO delivery systems that are responsive to the I/R damage microenvironment. Therefore, the development of a DFO-controlled release hydrogel system that is responsive to the acidic and MMP-2-rich microenviron-

https://doi.org/10.1021/acsami.5c02666
ACS Appl. Mater. Interfaces 2025, 17, 27906−27922

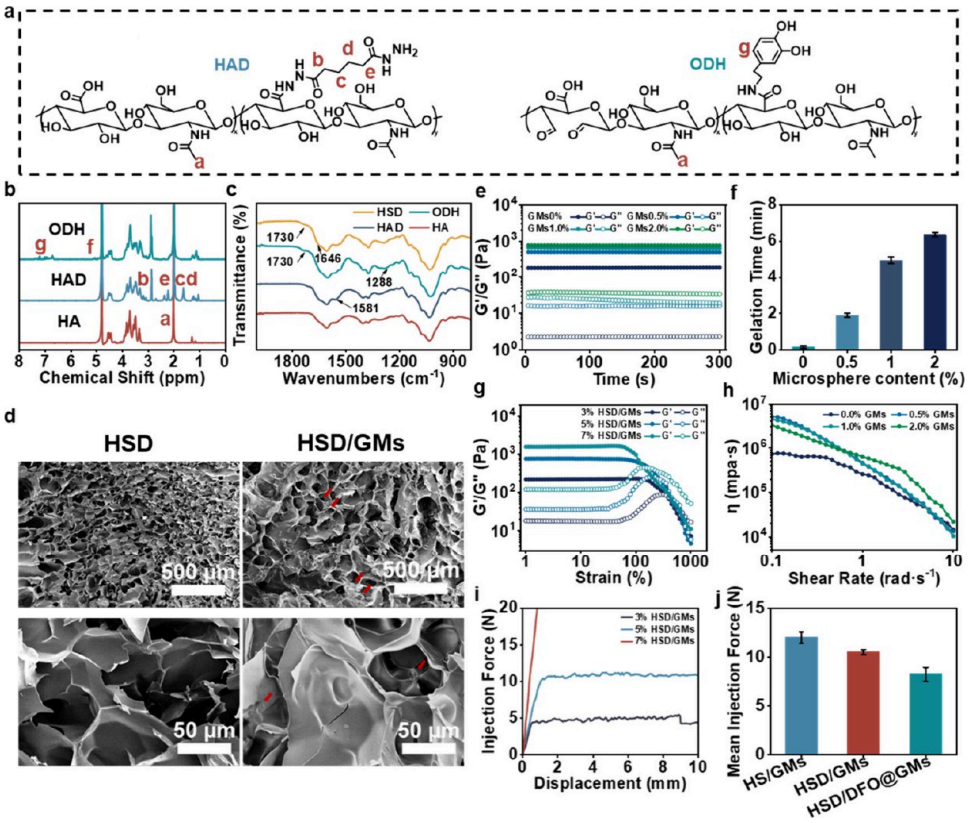

Figure 2. Formation and properties of HSD/DFO@GMs. (a) Structural formulas of HAD and the properties of ODH. (b) ^{1}H NMR spectra of HA, HAD, and ODH. (c) FT-IR spectra of HA, HAD, ODH, and HSD hydrogel. (d) SEM images of HSD and HSD/GMs hydrogel. (e) Rheological behaviors of HSD/GMs hydrogels with different GMs contents over 0−300 s at a constant frequency of 1 Hz and a strain of 20%. (f) Gelation time of HSD/GMs hydrogels with different GMs contents (n = 3). (g) Rheological behaviors of different hyaluronic acid derivatives content over a strain of 1−1000% at a constant frequency of 1 Hz. (h) Rheological behaviors of HSD/GMs hydrogels with different GMs contents over 0.1−10 rad·s^{-1}. (i) Injection force of HSD/GMs hydrogels with different hyaluronic acid derivatives contents. (j) Injection force of the HS/GMs, HSD/GMs, and HSD/DFO@GMs hydrogels (n = 3).

ment holds significant potential for cardiac applications by inhibiting ferroptosis and oxidative stress damage.

In this study, an injectable hydrogel based on HA derivative and DFO-loaded gelatin microspheres (DFO@GMs) was developed, featuring antiferroptosis properties and synergistic antioxidant capabilities, for the purpose of cardiac repair (Figure 1). First, dopamine-grafted oxidized hyaluronic acid (OHD) and adipic acid dihydrazide grafted HA (HAD) were synthesized. Meanwhile, DFO@GMs were constructed via emulsion cross-linking technology. Finally, the HA derivative-based hydrogel loaded with DFO@GMs (HSD/DFO@GMs) formed via the dynamic Schiff base bond between the aldehyde group in the OHD and amino groups in the HAD and DFO@GMs surface. The Schiff base bond and GMs can respond to the weakly acidic and MMP-2-rich microenvironments, respectively, thereby enabling the on-demand release of DFO in I/R-injured myocardium and reducing its cytotoxicity. Consequently, the HSD/DFO@GMs system is expected to exert comprehensive effects in inhibiting ferroptosis and oxidative stress damage owing to its unique composition and structure. Within this system, the HA main chain, DA side group, and released DFO can collectively chelate iron ions, thereby blocking the Fenton reaction and decreasing the LIP accumulation, which further inhibits the ferroptosis in cardiomyocyte. Additionally, the DA side group can also mitigate oxidative stress damage by scavenging ROS. These effects improve cardiac repair. To validate these scientific hypotheses, the formation of the injectable HSD/DFO@GMs hydrogel was investigated and the regulation law of composition on its physical and chemical properties was systematically explored, such as mechanical and injectable property, iron ion chelating ability, antioxidant activity, and degradation behaviors. Moreover, the release profiles of DFO from GMs and HSD/DFO@GMs were investigated under different pH values and a MMP-2-rich microenvironment. Building on these findings, the effects of HSD/DFO@GMs on ferroptosis and oxidant stress damage in H9C2 cells were subjected to hypoxia−reoxygenation (H/R) injury in vitro. Furthermore, the HSD/DFO@GMs hydrogel was injected into the I/R model rat to evaluate its microenvironment-regulation capability and repair effect on the damaged myocardium in vivo.

2. RESULTS AND DISCUSSION

2.1. Formation and Properties of Injectable Hydrogels with Ferroptosis Resistance and Antioxidant Capabilities. In this study, an injectable hydrogel that possesses antiferroptosis and antioxidant properties was designed and prepared. To control the release of DFO, gelatin microspheres loaded with DFO (DFO@GMs) were first prepared by using glutaraldehyde cross-linking. The resulting DFO@GMs displayed well-defined and closed structures, with an average size of 14.16 μm (Supporting Information Figure S1). The hydrophilic DFO was effectively encapsulated within

https://doi.org/10.1021/acsami.5c02666
ACS Appl. Mater. Interfaces 2025, 17, 27906−27922

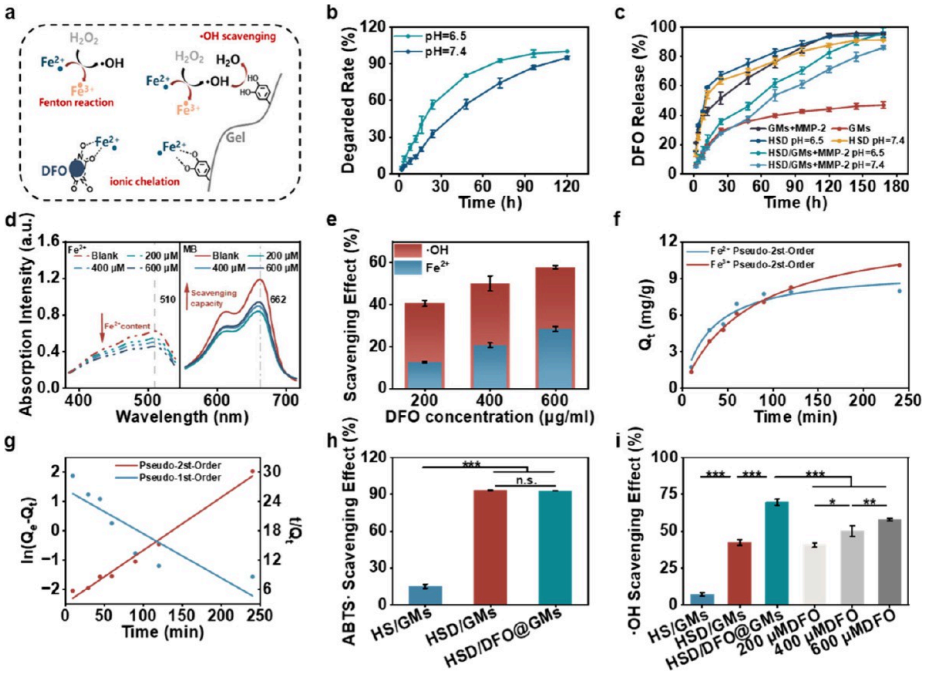

Figure 3. Iron ions scavenging and antioxidant effects of HSD/DFO@GMs. (a) Schematic illustration of iron ion chelation and ROS scavenging mechanism. (b) Degraded rate of the HSD/DFO@GMs in pH 7.4 and 6.5 solution (n = 3). (c) DFO released from GMs or hydrogels under different microenvironments (pH 7.4/6.5 and with/without MMP-2) (n = 3). (d) UV−vis absorbance spectra of remaining content of Fe^{2+} (left) and methylene blue oxidize (right) with different concentrations of DFO. (e) $^{\bullet}OH$ and Fe^{2+} scavenging effects of DFO with different concentration. (f) Pseudo-second-order kinetic fitting curves for Fe^{2+} and Fe^{3+} by HSD/GMs hydrogel (n = 3). (g) Comparison of pseudo-first-order and pseudo-second-order fits for the kinetic adsorption of Fe^{2+} by the HSD/GMs hydrogel. Scavenging effect of hydrogels against (h) ABTS· and (i) $^{\bullet}OH$ (n = 3; n.s., no significant difference; *p < 0.05; **p < 0.01; ***p < 0.001).

the GMs, and the encapsulation rate and drug loading rate of DFO in GMs depended on the DFO feed ratio. The Fe^{3+}−DFO standard curve was established to investigate DFO loading (Figure S2). As shown in Table S1, DFO@GMs exhibited high encapsulation efficiency (>63.72%), and the DFO loading rate in GMs increased from 0.979 ± 0.07% to 3.399 ± 0.09% when the DFO/GMs ratio was increased from 1.33% to 5.33%.

To improve the delivery efficiency and release behaviors of DFO, an injectable hydrogel based on HA was designed and prepared. First, OHD and HAD were synthesized (Figure 2a). The injectable HA-based hydrogel (HSD) was formed through the Schiff base bond between the aldehyde group in OHD and the amino group in HAD. The DA moieties were anticipated to enhance antioxidant performance. Furthermore, the DFO@GMs were incorporated into the HSD hydrogel to enhance the antioxidant activity and impart ferroptosis-inhibiting capabilities. FT-IR and ^{1}H NMR spectra were employed to confirm the chemical structures of ODH and HAD. As shown in Figure 2b, the characteristic chemical shifts of hydrazide methylene (1.53 ppm) were evident in the ^{1}H NMR spectrum of HAD, suggesting the successful synthesis of HAD with a 27% substitution degree of adipic acid dihydrazide in HA chain. Additionally, the N−H stretching vibration of sec-amide at 1581 cm^{-1} was observed in HAD compared to HA. In addition, the OHD spectrum exhibited characteristic adsorption bands, including a C═O stretching vibration at 1730 cm^{-1} and an amide III band at 1288 cm^{-1}. While the blue shift of the C═O stretching vibration at 1730 cm^{-1} to 1742 cm^{-1} indicates the incorporation of gelatin components in HSD/GMs (Figure S3). The characteristic chemical shifts ranging from 6.70 ppm to 6.90 ppm were attributed to the protons of the benzene ring in the dopamine side group. Meanwhile, the chemical shifts at 5.15 ppm and 5.6 ppm were assigned to the protons on the hemiacetals. These findings confirmed the successful synthesis of OHD, with the substitution degree of aldehyde and dopamine was measured as 44% and 30.5%, respectively, using hydroxylamine hydrochloride titration and UV spectrophotometry (Figure S4). When the HAD and ODH solution was mixed, HSD hydrogel was formed via the Schiff base reaction between the aldehyde groups in ODH and the amino groups in HAD. As shown in Figure 2c, the C═O stretching vibration of the aldehyde groups at 1730 cm^{-1} was attenuated in HSD hydrogel, while the C═N vibration at 1646 cm^{-1} was intensified compared to those in ODH. Macroscopically, the fluidity of two hydrogel precursors gradually decreased after mixing, eventually transitioning into a nonflowable hydrogel state (Figure S5). Moreover, the incorporation of DFO@GMs did not interfere with the gelation formation, and these DFO@GMs can uniformly disperse within the hydrogel (Figure 2d).

Rheological performance results showed that the storage modulus (G') of the HSD hydrogel was consistently higher than its loss modulus (G'') throughout the testing time frame (Figure 2e). The contents of GMs within the hydrogel can modulate both the gelation time and the mechanical property of the HSD hydrogel. As shown in Figure 2f, the gelatin time of HSD hydrogel was 0.17 ± 0.07 s. The introduction of GMs increased the gelatin time, which gradually increased from 1.9 ± 0.11 min to 6.35 ± 0.12 min as the GMs contents increased from 0.5% to 2.0%. Additionally, the incorporation of GMs can significantly enhance the mechanical property. The G' of HSD was 185.72 ± 12.35 Pa, and it increased to 755.57 ± 15.25 Pa when the GMs contents increased to 2%. This improvement is

https://doi.org/10.1021/acsami.5c02666
ACS Appl. Mater. Interfaces 2025, 17, 27906−27922

attributed to the increased overall solid content of the hydrogel. Additionally, the residual amino groups on the GMs surface could be the cross-linked site with the OHD, ultimately increasing the degree of cross-linking. In addition, the mechanical property increased with the solid contents in the hydrogel, as shown in Figure S6, the G' of HSD/GMs gradually increased to 219.42 ± 6.93 Pa from 1521.93 ± 16.00 Pa when the concentration of HSD increased 3% to 7%. The hydrogel maintains stable G' when the strain is less than 20% regardless of the solid contents (Figure 2g), indicating that the hydrogel can withstand the diastolic and systolic behavior of the heart (20%).[42]

Due to the dynamic nature of the Schiff base cross-linking structure, the prepared HSD/DFO@GMs hydrogel showed good injectable behaviors. The viscosity of the hydrogel rapidly decreased with the increasing shear rate (Figure 2h), decreasing by 2 orders of magnitude as the shear rate increased from 0.1 rad·s^{-1} to 10 rad·s^{-1} when its GMs content was 2%. Consequently, the hydrogel could be injected by a 1 mL needle after mixing using a double pass (Figure S7). When the hydrogel is extruded at a rate of 20 mm/min, the injection force gradually increased and reached a plateau period, which was defined as the injection force (Figure 2i). The injection force increased with the increase in the concentration of HA derivatives. Specifically, it was 4.45 and 10.52 N when the concentration of HA derivatives was 3% and 5%, respectively. These values facilitated easier manual handling and minimized the risk of surgical damage.[43] However, when the HA derivative concentration reached 7%, the injection force exceeded 20 N, making it less suitable for clinical operations. The addition of GMs and DFO@GMs did not significantly affect the injection forces. At a 5% solid content, the injection force remained approximately 10 N, regardless of the GMs content ranging from 0.5% to 2% (Figure S8a). Three kinds of hydrogels, HS/GMs, HSD/GMs, and HSD/DFO@GMs, were prepared at a ratio of 5% HA derivatives and 2% GMs, and all of their injection forces were less than 12 N (Figure 2j and Figure S8b).

2.2. Iron Ion Scavenging Effect and Antioxidant Properties. In the early stages of I/R injury, the loss or dysfunction of ferritin leads to an accumulation of excess LIP, which subsequently triggers ferroptosis. Additionally, these excess LIP ions can react with H_2O_2 through the Fenton reaction, generating a significant amount of ROS. It is expected that the HSD/DFO@GMs hydrogel can reduce LIP by controllably releasing DFO and leveraging the iron ion capture capability of the HSD network under an I/R injury microenvironment (Figure 3a). After I/R injury, the intratissue pH changed from 7.4 to a weakly acidic 6.5, accompanied by an increase in MMP-2 levels.[40,41] This microenvironment can modulate the degradation behaviors of the prepared HSD hydrogel and GMs, thereby controlling the release of DFO from the hydrogel. As shown in Figure 3b, HSD/DFO@GMs exhibited a higher degradation rate at pH 6.5 compared to pH 7.4, as Schiff base bonds are more unstable in weakly acidic microenvironments. For example, its degraded rate was 80.3 ± 1.04% at pH 6.5 on day 2, which was significantly higher than that at pH 7.4 (56.9 ± 3.87%). This provides a basis for modulating the release behaviors of DFO. To investigate DFO release behavior in the I/R injury microenvironment, experiments were conducted at pH 6.5 and 7.4, both with/without MMP-2. As shown in Figure 3c, the release of DFO from GMs was relatively low, with only 46.84 ± 2.07% released within 7 days. However, when DFO@GMs were immersed in an MMP-2 solution, the release rate significantly increased, with 51.50 ± 4.11% DFO released within the first 24 h and reaching 95.53 ± 0.76% by day 7. Direct incorporation of DFO into the HSD hydrogel resulted in burst release (63.54 ± 2.10% at pH 7.4 for 24 h and 66.97 ± 2.42% at pH 6.5) due to the degradation of HSD hydrogel. This burst release harms cardiomyocyte viability and impairs the hydrogel's therapeutic efficacy. The HSD/DFO@GMs system provided a dual-responsive release mechanism under an I/R injury microenvironment, achieving 35.60 ± 1.88% release at 24 h and 95.60 ± 3.62% by 7 days, thus preventing early burst release and late-stage incomplete release. The released DFO has the capability to rapidly chelate Fe^{2+}, thereby slowing down the rate of $^{\bullet}OH$ production. As shown in Figure 3d, the left panel demonstrates that in the absence of an oxidation reaction the scavenging rate of Fe^{2+} increases with higher concentrations of added DFO. In contrast, the right panel shows that, after introducing H_2O_2 to trigger oxidation, the oxidation of MB decreases as the DFO concentration increases. This phenomenon highlights DFO's primary mechanism for preventing ferroptosis: by blocking the iron required for the Fenton reaction, it reduces lipid peroxide production. As shown in Figure 3e, the scavenging effect of Fe^{2+} exhibited a trend similar to that of $^{\bullet}OH$ as the concentration of DFO was increased. Consequently, the deceleration of the reaction rate resulted in a higher scavenging effect of $^{\bullet}OH$ compared to that of Fe^{2+} at the same concentration. Additionally, the prepared HSD hydrogel can also bind to Fe^{2+} and Fe^{3+} due to its abundance of carboxyl groups and *o*-phenol structure. A certain volume of HSD/GMs was immersed in a 30 mg/L solution of Fe^{2+} or Fe^{3+}, and the residual concentration of Fe^{2+} or Fe^{3+} was determined at different times. Kinetic fitting was then conducted based on solid-state adsorption. As shown in Figure 3f,g and Figure S9, the adsorption of Fe^{2+} or Fe^{3+} by HSD/GMs approached equilibrium within approximately 4 h, and the pseudo-second-order model provided a better fit for both ions. This indicates that HSD/GMs can rapidly capture Fe^{2+} and Fe^{3+}. According to the fitting results of the pseudo-second-order model (Tables S3 and S4), the theoretical equilibrium adsorptions of HSD/GMs for Fe^{2+} and Fe^{3+} were 9.732 mg/g and 13.34 mg/g, respectively. Figure S10 illustrates the Fe^{2+}/Fe^{3+} chelating capacities of GMs, HS/GMs, and HSD/GMs. The adsorption amounts at 2 h and 4 h remained nearly constant, indicating equilibrium adsorption was achieved. HS/GMs exhibited significantly weaker Fe^{2+}/Fe^{3+} chelation compared to HSD/GMs. This suggests that while the anionic polysaccharide-based HS/GMs possess some iron-chelating ability, the dopamine (DA) component in HSD/GMs plays a dominant role in Fe^{2+}/Fe^{3+} chelation. These findings suggested that the HSD/GMs can serve to alleviate iron loading, thereby synergistically lowering the concentration of LIP in the cytosol.

The combined chelating effect of DFO and the hydrogel network on Fe^{2+} results in a reduction in the accumulation of the LIP, which subsequently leads to decreased production of ROS. To substantiate this effect, the scavenging capacities against 2,2-diphenyl-1-picrylhydrazyl radical (DPPH$^{\bullet}$), $^{\bullet}OH$, and 2,2′-azinobis (3-ethylbenzthiazoline-6-sulfonic acid) radical ion (ABTS$^{\bullet}$) free radicals were examined. As shown in Figure 3h,i and Figure S11, the HS/GMs hydrogel showed low antioxidant activity against the three types of ROS. The introduction of dopamine side group significantly improved the ROS scavenging effect, with the scavenging efficiencies of

https://doi.org/10.1021/acsami.5c02666
ACS Appl. Mater. Interfaces 2025, 17, 27906−27922

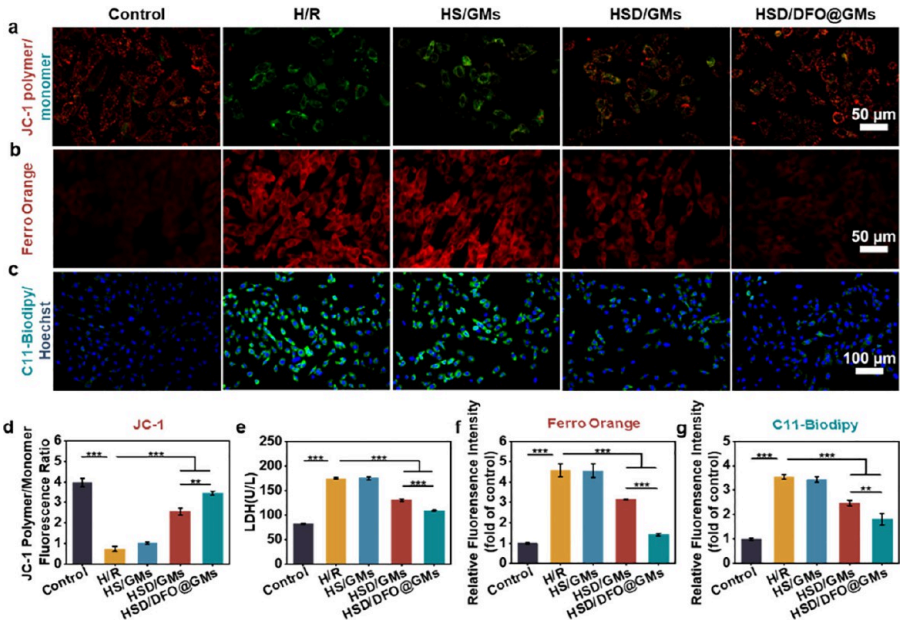

Figure 4. Inhibition of ferroptosis of cardiomyocytes in vitro. Fluorescence images of H9C2 cells stained by (a) JC-1 (polymer, red; monomer, green), (b) Ferro Orange (red) and (c) C11-Biodipy (green) undergoing H/R and different treatments. (d) Quantification of ratio of red to green fluorescence intensity represents the high and low mitochondrial membrane potentials (n = 3). (e) Quantification of LDH levels (n = 5). (f) Fe^{2+} concentration detected by Ferro Orange and (g) LPO level detected by C11-Biodipy (n = 3).

HSD/GMs reaching 68.40 ± 0.42% for DPPH•, 93.28 ± 0.17% for ABTS•, and 42.37 ± 1.93% for •OH. In addition, the HSD/DFO@GMs did not show significant differences with the HSD/GMs in the scavenging effects for DPPH• and ABST•. However, the introduction of DFO obviously improved the •OH scavenging capacity, further increasing it to 69.75 ± 1.99% for HSD/DFO@GMs, which was significantly higher than that of pure DFO (Figure 3i). We believe that the reason for this appearance is that •OH is generated by the Fenton reaction between Fe^{2+} and H_2O_2, and this Fenton reaction involving Fe^{2+} is the primary cause of oxidative stress damage due to iron imbalance in the cell.[14]

2.3. Inhibition of Ferroptosis and Oxidative Stress Damage of Cardiomyocyte In Vitro. The biocompatibility of the HSD/DFO@GMs hydrogel is a prerequisite for its successful in vivo application. As is well-known, DFO exhibits a certain cytotoxicity that depends on its concentration. As shown in Figure S12a,b and S13a,b, DFO did not have cytotoxicity toward H9C2 cells after 24 h of culture, regardless of the concentration. However, cell viability dropped below 80% at 48 h in the 200 μM DFO group. In contrast, when DFO was loaded into the HSD hydrogel, the H9C2 cells still demonstrated high cell viability in the HSD/DFO@GMs group (114.66 ± 9.61%) even with a DFO loading capacity of 1000 μM. This is primarily attributed to the controllable release behavior, which results in a lower local DFO concentration, thereby providing conditions for the long-term use of high-dose DFO. Additionally, due to the excellent biocompatibility of polysaccharide-based hydrogels, their extracts can promote cell proliferation and tend to exhibit higher cell viability than the control group. Furthermore, to evaluate the in vivo toxicity, the status of vital organs in rats was assessed 28 days after the hydrogel was injected into the damaged myocardium in I/R model rats. As shown in Figure S14, H&E staining revealed no pathological changes in the liver, spleen, lungs, or kidneys in any of the groups. Therefore, the prepared HSD/DFO@GMs hydrogel demonstrated excellent cellular and tissue compatibility.

Under H/R microenvironments, the viability of cardiomyocytes is significantly diminished as a result of ferroptosis and oxidative stress-induced damage. To investigate the inhibitory effects of the prepared HSD/DFO@GMs on ferroptosis and oxidative stress damage in cardiomyocytes, H9C2 cells were exposed to hypoxic (H) microenvironment (1% O_2) for 2 h followed by reoxygenation (R) for 12 h. In this H/R model, H9C2 cells exhibited unfavorable changes such as increased ROS and LPO content, upregulation of intracellular LIP, and mitochondrial membrane potential dysregulation. Compared to the control, the survival rate of H9C2 cells significantly reduced to 29.50 ± 2.19%. The introduction of HS/GMs did not change this damage, showing no statistical differences from the H/R group. As excepted, the cell survival rate significantly increased in HSD/GMs and HSD/GM@DFO group compared to the H/R group (p < 0.001), and the HSD/DFO@GMs group was able to recover the survival rate to 63.44 ± 5.10% (Figure S15). The H/R microenvironments also induced mitochondrial dysfunction; as shown in Figure 4a; a strong red fluorescence from JC-1 polymers was observed in normal H9C2 cells. In contrast, in the H/R and HS/GMs groups, this red fluorescence was replaced by green fluorescence, indicating the onset of cell apoptosis. However, the HSD/GMs group exhibited a significantly higher JC-1 polymer/monomer fluorescence ratio compared to H/R and HS/GMs groups (p < 0.001). Furthermore, the HSD/DFO@GMs group demonstrated the highest JC-1 polymer/monomer fluorescence ratio (p < 0.001 or p < 0.05) (Figure 4d). Consequently, a substantial amount of lactate dehydrogenase (LDH) was released from H9C2 cells under the H/R microenvironment. Notably, the HSD/DFO@GMs treatment significantly reduced the LDH release level (Figure 4e, p < 0.001), suggesting that the HSD/DFO@GMs hydrogel effectively decreased the H/R damage to H9C2 cells. This

https://doi.org/10.1021/acsami.5c02666
ACS Appl. Mater. Interfaces 2025, 17, 27906−27922

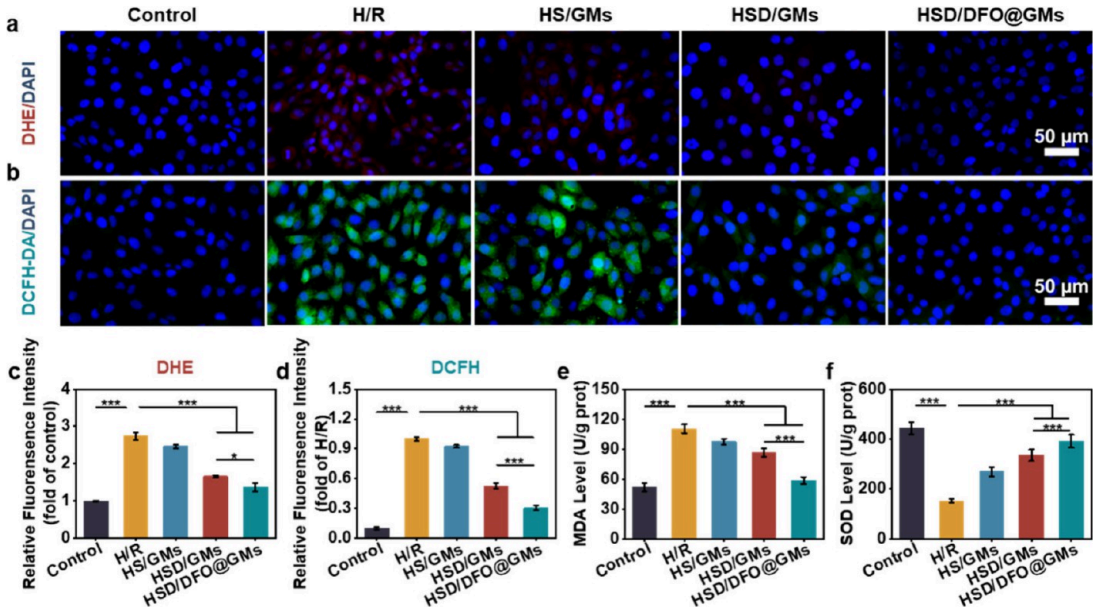

Figure 5. Inhibition of oxidative stress damage of cardiomyocyte in vitro. (a) Intracellular superoxide anion radical activity (DHE, red) and (b) total intracellular ROS (DCFH-DA, green). Quantification of ROS level detected by (c) DHE and (d) DCFH-DA (n = 3). Expression levels of (e) MDA and (f) SOD (n = 4). (*p < 0.05; **p < 0.01; ***p < 0.001).

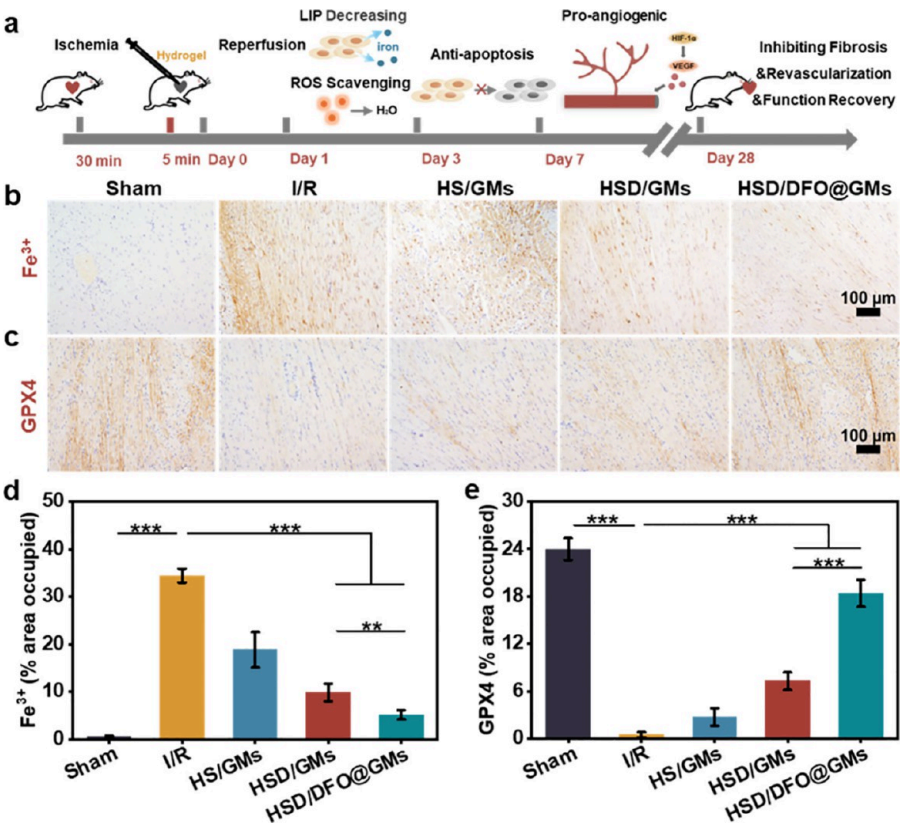

Figure 6. Inhibition of ferroptosis in vivo after I/R injury. (a) Schematic illustration of the therapeutic effect of hydrogels on I/R-injured hearts. Representative stained images of (b) Fe^{3+} and (c) GPX4 immunohistochemistry infarcted zone on day 1 after surgery. Quantitative analysis of (d) Fe^{3+} and (e) GPX4 area occupied. (n = 4; **p < 0.01; ***p < 0.001).

effect can be primarily attributed to its combined antiferroptosis and antioxidant properties.

To further elucidate the antiferroptosis effects, intracellular LIP levels were assessed by Ferro Orange staining. As shown in Figure 4b,f, a pronounced red Ferro Orange fluorescence was observed in H9C2 cells exposed to the H/R microenvironment, significantly exceeding that of the control group (p < 0.001). Notably, the HS/GMs treatment did not exert any discernible effects. Consistent with expectations, the most substantial decrease in LIP expression was evident in the

https://doi.org/10.1021/acsami.5c02666
ACS Appl. Mater. Interfaces 2025, 17, 27906−27922

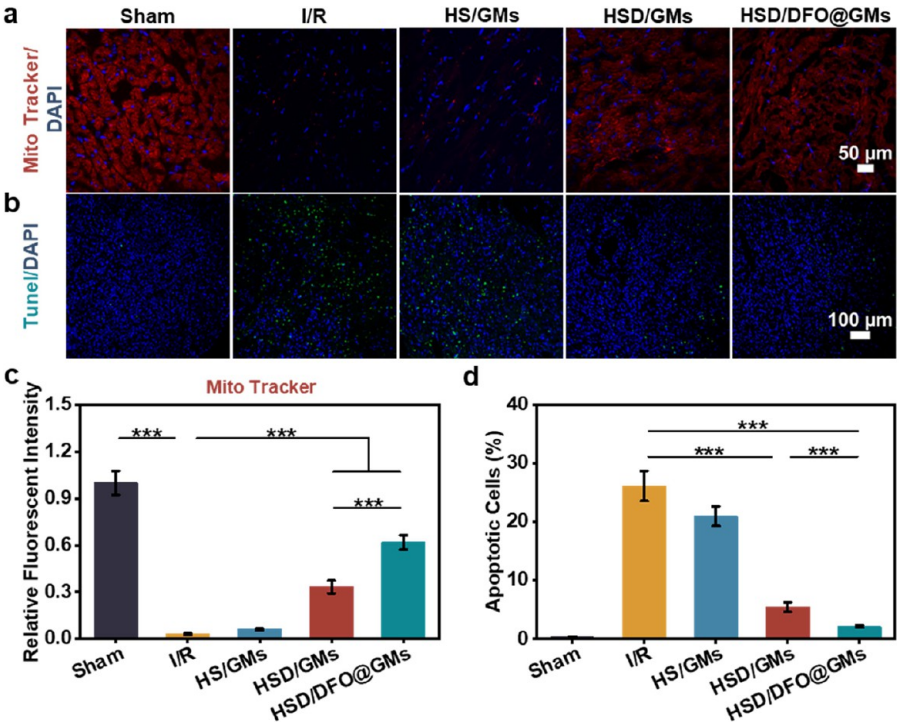

Figure 7. Inhibition of oxidative stress damage in vivo after I/R injury. (a) Representative fluorescent images of Mito Tracker at the infarcted zone on day 1 after surgery. (b) Representative fluorescent staining images of TUNEL at the infarcted zone on day 3 after surgery. (c) Relative fluorescent intensity of Mito Tracker standing at the infarcted zone. (d) Quantitative analysis of the apoptotic cell rate. (n = 4; ***p < 0.001).

HSD/DFO@GMs group compared to the H/R injury group. Disorders in LIP content can exacerbate in the intracellular Fenton reaction, leading to further oxidization to produce a large amount of LPO, thereby inducing ferroptosis. As shown in Figure 4c,g, ferroptosis probe C11-Biodpy, used as a marker of the cellular LPO, appeared around the nucleus of H9C2 cells in both H/R and HS/GMs groups. The DHS/DFO@GMs hydrogel can effectively inhibit the accumulation of LPO by reducing oxides and free iron ions, therefore resulting in significantly lower fluorescence intensity compared to other groups (p < 0.001 or p < 0.01). DFO promotes the activity and stability of HIF-1α by scavenging intracellular Fe^{2+}, thereby triggering the activation of a series of pro-angiogenic genes, including VEGFA. The H/R HUVECs cells were used to assess the expression levels of HIF-1α and VEGFA. As shown in Figure S16a,c, hypoxia treatment activated the cell's own antioxidant defense capacity, leading to upregulated levels of HIF-1α in the H/R group. Notably, the HSD/DFO@GMs group exhibited significantly higher expression levels of these markers compared to the other groups (p < 0.001), consistent with our measurements of intracellular LIP levels. Similarly, the HSD/DFO@GMs group improved the VEGFA expression (Figure S16b,d). These results suggest that HSD/DFO@GMs hydrogel promoted the expression of pro-angiogenic genes by HUVECs.

To elucidate the antioxidant effects, the expression of various ROS in the cytoplasm were determined using dihydroethidium (DHE) and 2′,7′-dichlorofluorescein (DCFH-DA) staining. As shown in Figure 5a,b, a significant decrease in fluorescence intensity in the HSD/GMs and HSD/DFO@GMs groups could be observed compared to the H/R control group (p < 0.001). As expected, differences were also noted between the DHS/DFO@GMs and HSD/DFO@GMs groups, particularly a significant difference in the fluorescence intensity of DHE, which reflects the overall ROS level (Figure 5c, p < 0.05), and a difference in the fluorescence intensity of DCFH-DA (Figure 5d, p < 0.001). In addition, the prepared HSD/DFO@GMs hydrogel can modulate the expression levels of malondialdehyde (MDA) and superoxide dismutase (SOD) in H9C2 after H/R damage. As shown in Figure 5e, compared with the control, the MDA expression level in the H/R group was higher than that of the control (p < 0.001). The addition of HSD/DFO@GMs attenuated this effect (p < 0.001). Similarly, the HSD/DFO@GMs stimulated SOD production, although it still was less than that in the control group, suggesting that HSD/DFO@GMs can effectively scavenge ROS and decrease the oxidative stress damage in H9C2 under the H/R microenvironment (Figure 5f).

2.4. Inhibition of Ferroptosis and Oxidative Stress Damage In Vivo after I/R Injury. Myocardial I/R injury is accompanied by the dysregulation of iron homeostasis and the generation of ROS, which culminate in ferroptosis by catalyzing the oxidation of phospholipids in various cellular membranes. It is anticipated that the prepared HSD/DFO@GMs hydrogel can effectively suppress ferroptosis and oxidative stress damage after I/R injury (Figure 6a). First, the Fe^{3+} deposition in cardiac tissue at the early stage of I/R injury was investigated, serving as an indicator of the total intracellular iron ions content. As shown in Figure 6b,d, a significant amount of Fe^{3+} was observed in the I/R group on day 1 postsurgery. However, the Fe^{3+} area was markedly reduced after treatment with HSD/GMs (p < 0.001). Furthermore, HSD/DFO@GMs led to an even greater decrease in Fe^{3+} deposition (p < 0.01), attributed to the synergistic Fe^{3+} scavenging action of the HSD network and DFO, which was consistent with the results of cellular experiments. In addition, the initiation of myocardial I/R injury is frequently associated with the downregulation of

https://doi.org/10.1021/acsami.5c02666
ACS Appl. Mater. Interfaces 2025, 17, 27906−27922

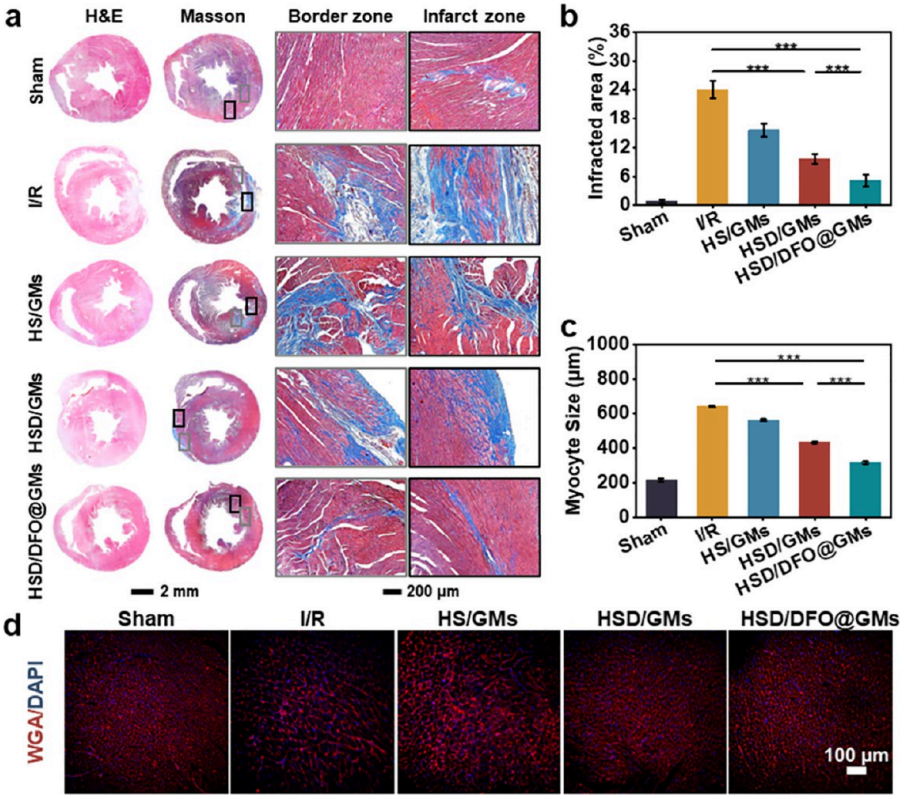

Figure 8. Modulation effects of HSD/DFO@GMs hydrogels on the morphology of the myocardium. (a) H&E and Masson's trichrome staining for muscle (red) and collagen (blue) in cardiac morphology. (b) Infarcted area fraction of LV. (c) Quantitative analysis of the myocyte size. (d) Representative fluorescent staining images of WGA at the border zone on day 28 after surgery. (n = 4; ***p < 0.001).

glutathione peroxidase 4 (GPX4), suggesting a breakdown in the intracellular ferroptosis defense mechanisms.[44] As shown in Figure 6c,e, the expression level of GPX4 markedly increased following I/R injury compared to the Sham group (p < 0.001). As expected, the HSD/DFO@GMs hydrogel group showed the highest GPX4 expression (p < 0.001). As shown in Figure S17a,c ASCL4, a negative regulator of ferroptosis, exhibited inverse trends compared to GPX4. Notably, the expression of ASCL4 was significantly downregulated in the HSD/DFO@GMs hydrogel group, reaching its lowest level (p < 0.001), in stark contrast to the elevated levels observed post-I/R injury. Furthermore, the concentration of the lipid peroxidation marker 4-HNE (Figure S17b,d) was markedly reduced in the HSD/DFO@GMs hydrogel group compared to other groups (p < 0.001), suggesting a considerable decrease in lipid peroxide accumulation. These findings suggest that HSD/DFO@GMs may mitigate regional iron deposition in myocardial tissues by modulating the expression of cellular ferroptosis-related proteins, thereby lowering the risk of ferroptosis in the I/R region. This finding suggested that HSD/DFO@GMs can reduce the risk of ferroptosis in I/R area by modulating the expression levels of cellular ferroptosis inhibitory proteins positively and by reducing regional iron deposition in myocardial tissue.

The HSD/DFO@GMs hydrogel demonstrates a significant capacity to mitigate oxidative stress damage following I/R injury by modulating the ROS microenvironment. As shown in Figure S18a–d, the fluorescence intensity of DHE and DCFH-DA in the HSD/DFO@GMs group was markedly reduced, substantially lower than that observed in another group (p < 0.001 or p < 0.05), suggesting hydrogel's efficacy in scavenging ROS in vivo post-I/R injury. Therefore, this action alleviates mitochondrial damage caused by ROS. As shown in Figure 7a, the fluorescence signal of Mito Tracker was nearly an undetectable post-I/R injury compared with that of the Sham group. However, treatments with HSD/GMs and HSD/DFO@GMs preserved mitochondrial integrity. Notably, the HSD/DFO@GMs group exhibited a significantly higher relative fluorescence intensity than other groups (p < 0.001), although it remained lower than that of the Sham group (Figure 7c). The serum levels of MDA and SOD were investigated in each group of rats. As shown in Figure S19a,b, the addition of HSD/DFO@GMs reduced the expression level of MDA compared to the I/R group (p < 0.001). Similarly, SOD production was stimulated, indicating that HSD/DFO@GMs effectively scavenged ROS and reduced oxidative stress damage in the microenvironment after I/R.

The degree of apoptosis, distinct from ferroptosis, within the I/R injury infarcted area was also assessed. TUNEL staining revealed that 26.2 ± 2.59% of cardiomyocytes underwent apoptosis due to the dysregulation of the microenvironment following I/R injury (Figure 7b,d). In contrast, the rate of apoptosis-positive cardiomyocytes was significantly reduced to 5.48% and 2.17% after treatment with HSD/GMs and HSD/DFO@GMs hydrogels, respectively. In addition, HSD/DFO@GMs treatment significantly reduced serum LDH levels (Figure S20, p < 0.001), suggesting that HSD/DFO@GMs effectively prevented the massive apoptosis of cardiomyocytes after I/R. Therefore, the HSD/DFO@GMs alleviates oxidative stress and reduces both apoptosis and ferroptosis in the early stages of I/R injury through the synergistic antioxidative of

https://doi.org/10.1021/acsami.5c02666
ACS Appl. Mater. Interfaces 2025, 17, 27906−27922

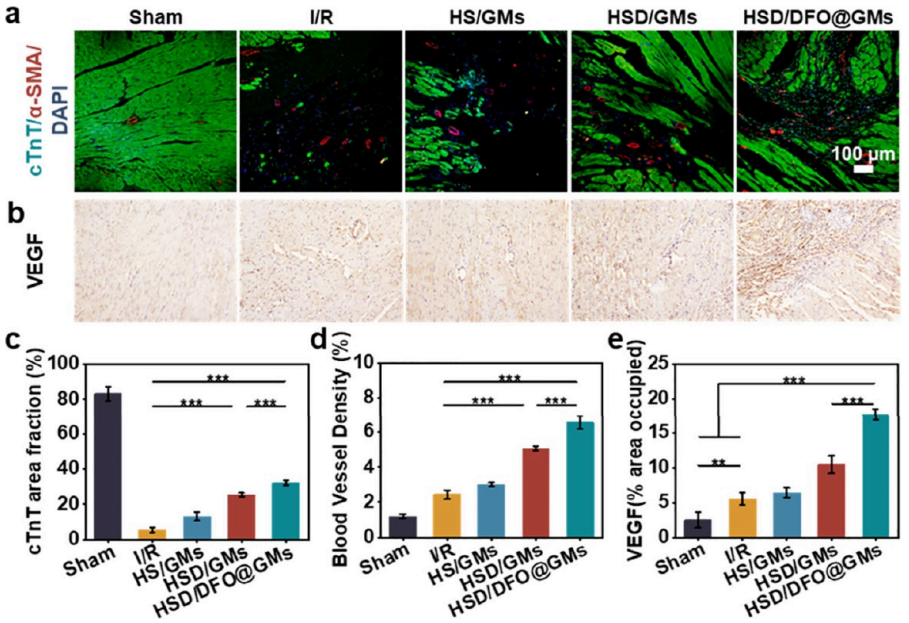

Figure 9. Modulation effects of HSD/DFO@GMs hydrogels on the function of the myocardium. (a) Representative immunofluorescence staining images of cTnT (green), α-SMA (red), and DAPI (blue) at the infarcted zone on day 28 after surgery. (b) Representative images of VEGF immunohistochemistry. Quantitative analysis of the (c) cTnT area fraction and (d) blood vessel density. (e) Quantitative analysis of the VEGF areas occupied. (n = 4; $^{**}p < 0.01$; $^{***}p < 0.001$).

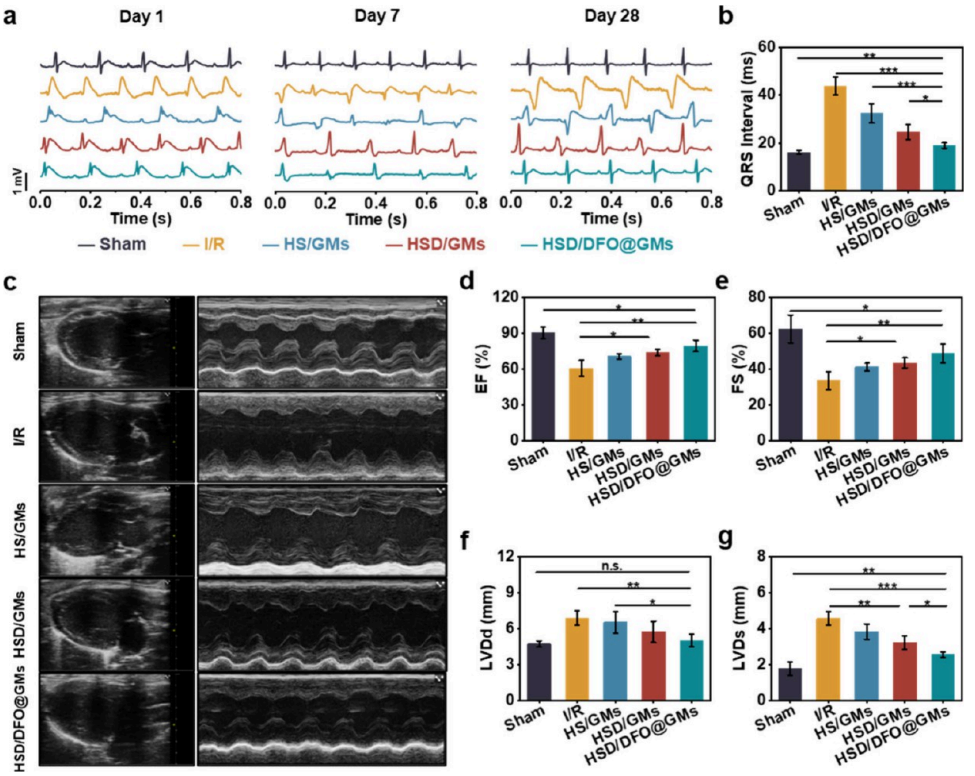

Figure 10. Cardiac electrophysiology and systolic function. (a) Representative ECGs for rats in different groups at 1, 7, and 28 days postoperatively. (b) QRS interval duration. (c) Echocardiography imaging of rats in different groups after 28 days. (d) EF, (e) FS, (f) LVDd, and (g) LVDs on 28 days after surgery (n = 4; n.s., no significant difference; $^{*}p < 0.05$; $^{**}p < 0.01$; $^{***}p < 0.001$).

dopamine moiety and DFO, providing recovery of cardiac function in the maturation phase.

2.5. Therapeutic Efficacy of the HSD/DFO@GMs Hydrogel on Cardiac I/R Injury in Rats. Due to the mitigated effects of ferroptosis and oxidative stress damage, we hypothesized that the prepared HSD/DFO@GMs hydrogel could effectively decrease myocardial infarction area in the I/R-injured region. To verify this effect, LV remodeling was assessed by H&E and Masson's trichrome staining on day 28 postsurgery. As shown in Figure 8a, the Sham group exhibited normal red myocardial tissue, while the I/R group displayed LV dilatation and a significant number of blue-stained

https://doi.org/10.1021/acsami.5c02666
ACS Appl. Mater. Interfaces 2025, 17, 27906−27922

fibroblasts and collagen deposits. The collagen deposition significantly decreased in all of the hydrogel treatment groups. In addition, Figure 8b showed that the infarct area in the HS/GMs group was significantly lower than that of the I/R group ($p < 0.001$), which may be attributed to the fact that the HA has an extracellular matrix-like composition,[45] as well as the fact that the hydrogel provided mechanical support in place of dead cardiomyocytes.[46] HSD/GMs and HSD/DFO@GMs hydrogel reduced the infarct area to 9.66 ± 1.06% and 5.15 ± 1.20% compared to HS/GMs due to antiferroptosis and suppression effects of oxidative stress damage. Meanwhile, the HSD/DFO@GMs hydrogel can also reduce the compensatory hypertrophy of cardiomyocytes. Wheat germ agglutinin (WGA) staining suggested that the cardiomyocytes surrounding the infarcted area were significantly enlarged in the I/R group compared to those in the Sham group, with evidence of cell membrane damage. All hydrogel treatment groups inhibited cardiomyocyte hypertrophy, showing significantly smaller myocyte sizes than the I/R group ($p < 0.001$). The HSD/DFO@GMs group demonstrated the greatest inhibitory effect, attributed to the preservation of more intact myocardial tissue (Figure 8c, 8d).

I/R induced a significant decrease in cardiac troponin T (cTnT) expression in cardiomyocyte, making it difficult to observe green cTnT positive cells in the I/R group (Figure 9a,c). All hydrogel treatments increased the percentage of cTnT-positive cells. The HSD/DFO@GMs group exhibited the highest cTnT expression level ($p < 0.001$) compared with other groups, with more regular alignment of cardiomyocytes, suggesting higher survival rates of cardiomyocytes in the I/R-injured area. Restoration of the vascular network in the I/R-injured area is a crucial factor for recovering cardiac function at maturity.[47] Vessel formation in the infarcted region was assessed using α-smooth muscle actin (α-SMA) staining (Figure 9a,d). The vessel density was higher in the I/R and HS/GMs groups compared with the Sham group, which was attributed to spontaneous recruitment of endothelial cells in the infarcted region. The HSD/GMs group showed increased vessel density, likely due to reduced oxidative stress in the early stage. The HSD/DFO@GMs group exhibited the highest vessel density, which can be attributed to pro-angiogenic effects of released DFO. DFO inhibits prolyl hydroxylase and promotes the activity and stability of HIF-1α by chelating intracellular Fe^{2+} and stimulates activation of a range of pro-angiogenic genes, including vascular endothelial growth factor.[30,31] The expression levels of HIF-1α and VEGF were measured at 7 d postprocedure (Figure 9b, 9e, S21a-b), with the HSD/DFO@GMs group showing significantly higher levels compared to other groups. These results suggested that the sustained slow release of DFO facilitates restoration of vascular network in the infarcted area.

The cardiac electrophysiological responses were monitored through the acquisition of electrocardiograms (ECGs) on postoperative days 1, 7, and 28. As shown in Figure 10a,b, the ECGs from all groups subjected to I/R injury exhibited a significant ST-segment elevation on day 1, which is indicative of acute myocardial injury. On days 7 and 28 after surgery, the proliferation of fibrotic tissue led to characteristic changes in the ECGs of the I/R and HS/GMs groups, such as deepening of the Q wave, inversion of the T wave, and prolongation of the QRS interval. These alterations suggested a progressive impairment of electrophysiological conduction with cardiac tissues. In contrast, the early removal of ROS and excess irons in thHSD/DFO@GMs group preserved a substantial number of viable cardiomyocytes. Consequently, this group demonstrated reduced QRS intervals and mitigated electrical decoupling and arrhythmia in the infarcted area, which was significantly lower compared to other groups ($p < 0.001$ vs I/R and HS/GMs, $p < 0.05$ vs HSD/GMs), although it was still slightly higher than that in the Sham group ($p < 0.01$).

Echocardiography was used to evaluate cardiac diastolic and systolic function, as well as the degree of ventricular dilatation after 28 days postsurgery. As shown in Figure 10c, in comparison to the Sham group, both the I/R and HS/GMs groups exhibited LV thinning and diminished systolic activity, because of malignant remodeling of the ventricles. Treatment with HSD/DFO@GMs restored heart function to levels comparable to those the Sham group. The ejection fraction (EF) and fractional shortening (FS) values significantly decreased in the I/R group to 60.74 ± 6.69% and 33.60 ± 5.06%, respectively, from 90.35 ± 4.71% and 62.40 ± 7.78% in the Sham group (Figure 10d,e). All hydrogels improved ventricular dilatation by mechanical support, with both EF and FS increasing the injection of HS/GMs, HSD/GMs, and HSD/DFO@GMs hydrogel. Benefiting from its antioxidant and antiferroptosis effects, the HSD/DFO@GMs group achieved the highest values (EF, 79.47 ± 4.75%; FS, 48.76 ± 5.44%). Furthermore, various parameters of the LV further elucidate these effects (Figure 10f,g and Figure S22a,b), including LV end-systolic diameter (LVDs), LV end-diastolic diameter (LVDd), LV end-systolic volume (LVS), and LV end-diastolic volume (LVD). I/R injury increased the LVDd (6.88 mm) and LVDs (4.56 mm) compared to the Sham group. However, the injection of HSD/DFO@GMs decreased this trend, reducing LVDd to 4.99 mm, with no statistically significant difference compared to the Sham group.

3. CONCLUSIONS

In this study, an injectable HSD/DFO@GMs hydrogel antiferroptosis and antioxidant properties for cardiac repair was design and prepared. This hydrogel effectively chelated Fe^{2+} after I/R injury through its HA network and the release of DFO. Additionally, it can effectively scavenge the ROS via DA side groups and released DFO, thereby providing a suitable microenvironment for the repair of the damaged myocardium. Results suggested that the prepared HSD/DFO@GMs hydrogel favorable injectability due the Schiff base dynamic covalent cross-linking structure between aldehyde group in ODH and amino in HAD and GMs. Additionally, the HSD/DFO@GMs showed stable mechanical property and the mechanical strength can be modulated by ODH/HAD concentration and GMs contents. Moreover, the cross-linked structure and gelatin matrix can respond to the weak acid microenvironment and MMP-2 after I/R injury, achieving controlled release of DFO. Therefore, the prepared hydrogel can effectively inhibit the ferroptosis and oxidative stress damage of H9C2 cardiomyocyte under H/R microenvironment. When the HSD/DFO@GMs hydrogel was injected into the I/R-injured myocardium, it synergistically attenuated oxidative stress in the infarcted region, adjusted intracellular LIP content and ferroptosis regulator levels, and facilitated promotes revascularization, ultimately leading to the restoration of cardiac beat function. Overall, this work provides a possible approach for the treatment of I/R myocardial tissue injury by inhibiting ferroptosis and oxidative stress damage in cardiomyocyte.

https://doi.org/10.1021/acsami.5c02666
ACS Appl. Mater. Interfaces 2025, 17, 27906−27922

4. EXPERIMENTAL SECTION

4.1. Materials. Gelatin (Type A from Porcine, 250 Bloom), hyaluronic acid (HA, 9−10 kDa), adipic acid dihydrazide (ADH, 99%), 1-hydroxybenzotriazole (HOBT, 98%), dopamine hydrochloride (DA-HCl, 98%), *N*-(3-(dimethylamino)propyl)-*N*′-ethylcarbodiimide hydrochloride (EDC, 97%), and *N*-hydroxy succinimide (NHS, 98%) were purchased from Aladdin (Shanghai, China). Deferoxamine mesylate (DFO, 98%) and sodium periodate (99%) were purchased from Meryer (Shanghai, China). Collagenase II, Recombinant Human MMP-2 and CCK-8, LDH, ABTS, MDA, and SOD free radical scavenging kits were purchased from Solarbio (Shanghai, China). Hoechst 33342, C11-Biodipy, and JC-1 kits were purchased from Beyotime (Shanghai, China). Ferrous Ion Detection Kit (Ferro Orange) was purchased from Maokang Bio (Wuhan, China).

4.2. Synthesis of DFO-Loaded Gelatin Microspheres. DFO-loaded gelatin microspheres (DFO@GMs) were prepared by employing an emulsion cross-linking method. Briefly, a 15 wt % gelatin solution was dropped into the oil phase, which consisted of 60 mL of liquid paraffin and 1 g of SP-80, utilizing a device designed for constant velocity injection. The mixed solution was emulsified at 60 °C under stirring, followed by cooling in an ice bath. Subsequently, 1.5 mL of glutaraldehyde solution (25% (v/v)) was added to the emulsion, and the reaction was carried out under stirring for 1 h. The reaction mixture was then dehydrated by the addition of 80 mL of acetone and stirring for 30 min. After filtration, the GMs were obtained and washed alternately with anhydrous ether and acetone to remove the oil phase. The GMs were placed in a vacuum drying oven for 24 h. Finally, the GMs were redispersed in aqueous solution and dropped into $NaBH_4$ aqueous (4 wt %). The GMs were filtered, washed three times with deionized water, dehydrated by adding anhydrous ethanol, and finally placed in a vacuum drying oven for another 24 h. To load DFO, varying amounts of DFO (20 mg, 50 mg, and 80 mg) were incorporated into the gelatin solution and the DFO@GMs were prepared using the same method. The morphology was observed by SEM (Regulus 8100, HITACHI, Japan), and the size was counted.

4.3. Characterizations of DFO-Loaded Gelatin Microspheres. In order to determine the amount of DFO loading, a DFO-Fe^{3+} standard curve was established. Then, 5 mg of DFO@GMs was suspended in a collagenase II solution (0.6 mg/mL) at 40 °C for 30 min. The supernatant was added to a 96-well plate with a drop of 3 mM $FeCl_3$ solution, the absorbance was measured after 5 min of standing time, with GMs used as a control, and the eqs 1 and (2) were used to calculate the loading and encapsulation rates.[48]

$$\text{DFO loading capacitiy} = \frac{\text{weight of DFO in DFO@GMs}}{\text{weight of DFO@GMs}} \times 100\% \quad (1)$$

$$\text{encapsulation efficiency} = \frac{\text{weight of DFO in DFO@GMs}}{\text{weight of DFO fed initially}} \times 100\% \quad (2)$$

4.4. Preparation of Injectable HSD/DFO@GMs Hydrogel. First, dopamine-grafted oxidized hyaluronic acid (OHD) was synthesized. Briefly, 3 g of HA was dissolved in 100 mL of deionized water, and 2.4 g of sodium periodate was added and stirred in the dark. After 2 h, the reaction was terminated by the addition of 5 mL of ethylene glycol for 2 h, dialyzed against deionized water (MWCO 8000−14000) for 3 days, and freeze-dried to obtain oxidized hyaluronic acid (OHA). Then, 1 g of the prepared OHA was dissolved in 100 mL of MES buffer (0.1 M), and 1 g of EDC-HCl and 0.3 g of NHS were added under stirring for 30 min. A 0.5 g amount of DA-HCl was added under N_2 atmosphere to adjust the pH to about 4.7. After 10 h, the product was sequentially treated with 1 M NaCl solution, HCl solution (pH 5.0), and deionized water, followed by freeze-drying to yield OHD. For the synthesis of adipic acid dihydrazide grafted HA (HAD), 1 g of HA was completely dissolved in 100 mL of MES buffer (0.1 M) and then 1.36 g of HOBT and 1.15 g of EDC-HCl were added to the HA solution; the pH value was adjusted to 6.0 using 0.1 M NaOH. After 1 h. 4.36 g of ADH was added. The reaction was carried out for 48 h. The reaction solution was dialyzed against deionized water for 5 days and then was freeze-dried to obtain HAD. The chemical structures of OHD and HAD were determined by ^{1}H NMR spectroscopy (AVANCE IIITM HD 400 MHz, Bruker, Germany), FI-TR (iS50), and titration with hydroxylamine hydrochloride.[43]

The prepared HAD and ODH were dissolved in deionized water to form a final concentration of 5 wt %, respectively. Then, the obtained HAD and ODH aqueous solutions were mixed at 1:2 volume ratios to prepare the HSD hydrogel. GMs or DFO@GMs were dispersed in HAD solution to prepare HSD/GMs or HSD/DFO@GMs hydrogel with a final concentration of 2 wt % GMs. Using the same method, the HS/GMs, HSD/GMs, and HSD/DFO@GMs with different GMs contents and HA contents were prepared; the detail prepared parameters were list in Table S2.

4.5. Characteristics of HSD/DFO@GMs Hydrogel. The morphology and microstructure of the HSD and HSD/DFO@GMs hydrogels were investigated by SEM (Apreo S LoVac). The chemical structures and physical interactions of HSD/DFO@GMs were investigated by FI-TR (iS50).

The rheological properties of the HSD/DFO@GMs hydrogels were evaluated at a physiological temperature of 37 °C by using a rheometer (MCR302, Anton Paar) equipped with 25 mm parallel plates. The storage modulus (G') and loss modulus (G'') of the stabilized HSD/DFO@GMs hydrogel were determined through a time sweep ranging from 0 to 300 s at a frequency of 1 Hz and a constant strain of 20%. The gelation time was ascertained via time sweep and vial inversion; the gelatin time is defined as the point at $G' = G''$. The shear thinning behaviors of the prepared hydrogels were evaluated by increasing the shear rate from 0.1 rad/s by 10 rad/s. To ascertain the yield strain of the prepared hydrogel, strain sweeps were conducted from 0 to 1000% at a constant frequency of 1 Hz.

The injectability of the HSD/DFO@GMs hydrogel was assessed by using a universal electromechanical tester equipped with a 50 N load cell (WDW-05, Si Pai, Inc., China). A 1 mL syringe filled with HSD/DFO@GMs hydrogel precursor solution with different solid contents (3%, 5%, and 7%) and DFO@GMs (0.5%, 1.0%, and 2%) was fixed to the tester. The hydrogel was injected through an 18G needle at a controlled rate of 20 mm/min. The force−displacement curves were meticulously recorded with the mean value of the plateau region being designated as the representative injection force for the hydrogel.

4.6. Measurement of Antioxidant Efficiency. The antioxidant efficiency of the HSD/DFO@GMs hydrogels was evaluated by determining the scavenging efficiency against free radicals of DPPH$^\bullet$, the hydroxyl radical $^\bullet$OH, and ABTS$^\bullet$. All of the DFO was directly added into the HSD hydrogel. For the DPPH$^\bullet$ assay, 200 μL of hydrogel was incubated with 2 mL of DPPH$^\bullet$ ethanol solution (0.4 mM) in a shaker at 37 °C for 30 min, 60 min, 90 min, and 120 min. An equal amount of deionized water was used instead of the hydrogel as a control. The absorbance of the supernatant was measured at 517 nm by using an enzyme marker (Infinite 200pro, TECAN, Switzerland). The DPPH$^\bullet$ scavenging effect was calculated by the eq 3, where $A_{control}$ and A_{sample} are the absorbances at 517 nm of the supernatant of the hydrogel and control groups, respectively.

$$\text{DPPH}^\bullet \text{ scavenging effect (\%)} = \frac{A_{control} - A_{sample}}{A_{control}} \times 100 \quad (3)$$

The scavenging effect of $^\bullet$OH radicals was evaluated by using the Fenton reaction and the colorimetric change of methylene blue (MB). Briefly, 200 μL of HSD/DFO@GMs hydrogel or DFO solution was added into a mixture containing 400 μL of $FeSO_4$ (1.8 mM) and H_2O_2 (1.5 mM) solution, to which 400 μL of methylene blue solution was added. The resulting mixture was incubated at 37 °C for 30 min. Equal amounts of deionized water were used instead of the hydrogel

https://doi.org/10.1021/acsami.5c02666
ACS Appl. Mater. Interfaces 2025, 17, 27906−27922

as the blank group, and deionized water was used in place of both the $FeSO_4$ solution and the hydrogel as the control. The absorbance of the supernatant at 662 nm was then measured using an enzyme marker.[48] The •OH scavenging effect was calculated according to eq 4, where A_{sample}, A_{blank}, and $A_{control}$ were the absorbances of the supernatant in hydrogel, blank, and control group, respectively.

$$\text{•OH scavenging effect (\%)} = \frac{A_{sample} - A_{blank}}{A_{control} - A_{blank}} \times 100 \quad (4)$$

In addition, the ability of the hydrogel to clear ABTS• was determined by referring to the method provided in the kit. Briefly, 150 μL of HSD/DFO@GMs hydrogel was taken and its absorbance of the supernatant at 405 nm was determined. The ABTS• scavenging effect was calculated according to the eq 5, where A_{sample}, A_{blank}, and $A_{control}$ are the absorbances of the supernatant in hydrogel sample, blank, and control group, respectively.

$$\text{ABTS• scavenging effect (\%)} = \frac{A_{control} - A_{sample}}{A_{control}} \times 100 \quad (5)$$

4.7. Detection of Scavenging Effect for Divalent Iron Ions. In order to determine the scavenging effects of DFO for Fe^{2+}, 1,10-phenanthroline solution was added to a mixed solution of DFO and $FeSO_4$ and the absorbance of the supernatant at 510 nm was measured using an enzyme marker according to a previous report.[49] The DFO solution was replaced by an equal amount of deionized water or 1,10-phenanthroline solution as the control group and blank group, respectively. The Fe^{2+} scavenging effect was calculated using the eq 6, where A_{sample}, A_{blank}, and $A_{control}$ are the absorbance at 510 nm of the supernatant of the hydrogel sample, blank, and control group, respectively.

$$Fe^{2+}\text{ scavenging effect (\%)} = \frac{A_{control} - A_{sample}}{A_{control} - A_{blank}} \times 100 \quad (6)$$

4.8. Degradation Property Test. The HSD/DFO@GMs hydrogels were subjected to lyophilization to obtain a dry state. Approximately 20 mg (denoted as w_0) of the lyophilized hydrogel was then immersed into 2 mL of deionized water, adjusted to either pH 6.5 or pH 7.4. These hydrogel samples were incubated in a shaker (37 °C, 80 rpm) for a predetermined duration. Following incubation, the weight of the hydrogel (w_t) was ascertained postlyophilization. The degradation rate was calculated according to eq 7:

$$\text{degradation rate (\%)} = \frac{w_0 - w_t}{w_0} \times 100 \quad (7)$$

4.9. Determination of DFO Release Behaviors. To assess the release kinetics of DFO under different conditions, a 3 mM $FeCl_3$ solution was introduced into a DFO solution of different concentrations. The resulting standard curve was constructed by measuring the absorbance at 446 nm with an enzyme marker after 30 min. Subsequently, 5 mg of DFO@GMs was added into 8 mL of deionized water, either with or without the addition of MMP-2 (20 nM). These samples were incubated in a shaker at 37 °C and 100 rpm for 7 days. At regular intervals, 100 μL of supernatant was collected and the concentration of DFO was determined using the aforementioned method, with an equal volume of the corresponding solution being replenished to maintain the system's integrity. Similarly, HSD/DFO and HSD/DFO@GMs were added into 8 mL of deionized water (pH = 6.5 or 7.4) and the DFO concentration was determined by the above method. According to a previous report,[50] the cumulative release rate (E_r) of DFO was calculated according to eq 8, where V_e is the volume of supernatant removed at each interval; V_0 is the total volume of the solvent; C_i is the concentration of the DFO extracted at the Ith interval; and m_{DFO} is the total mass of DFO.

$$E_r = \frac{V_e \sum_{i=1}^{n-1} C_i + V_0 C_n}{m_{DFO}} \times 100 \quad (8)$$

4.10. Fe^{2+} and Fe^{3+} Adsorption Kinetics Experiments. First, $FeSO_4$ and $FeCl_3$ solutions with different Fe^{2+} or Fe^{3+} concentrations (5 mg/L, 10 mg/L, 20 mg/L, 30 mg/L, 50 mg/L, and 100 mg/L) were prepared and mixed with 1,10-phenanthroline and KSCN solutions, respectively. The absorbances at 510 nm and 480 nm were measured using an enzyme marker to construct the standard curves. Subsequently, about 10 mg of HSD/GMs was added into 10 mL of $FeSO_4$ solution and incubated in a shaker at 37 °C for different durations (10 min, 30 min, 45 min, 60 min, 90 min, 120 min, and 240 min). The immediate adsorptions of Fe^{2+}/Fe^{3+} by HS/GMs hydrogels and GMs at 2 h and 4 h were measured using the same method. The Fe^{2+} concentration was then measured by using the above method. Fe^{3+} kinetic adsorption was determined by using the aforementioned method. The theoretical equilibrium adsorption amount (Q_e) was determined using variation equ 9. The process was fitted with a pseudo-first-order model (Lagergren eq 10) based on solid-phase adsorption capacity. Then, a pseudo-second-order model (Ho eq 11) was applied, referencing the results from the pseudo-first-order fit,[51] where Q_t is the adsorbed amounts (mg/g) at time t and k_1 and k_2 are the rate constants.

$$Q_t = Q_e(1 - \exp(-k_1 t)) \quad (9)$$

$$\log(Q_e - Q_t) = \log Q_e - k_1 t \quad (10)$$

$$\frac{t}{Q_t} = \frac{1}{k_2 Q_e^{\,2}} + \frac{t}{Q_e} \quad (11)$$

4.11. Cytotoxicity Assay. The cytocompatibilities of HSD/DFO@GMs and DFO were assessed by Acridine Orange (AO) staining and the CCK-8 assay (CA1210, Solarbio) using H9C2 mouse cardiomyocytes. ODH, HAD, and DFO@GMs were sterilized via UV irradiation, and the hydrogel extracts were prepared by immersing 1 mL of the HSD/DFO@GMs hydrogel in 10 mL of complete medium at 37 °C for 48 h. H9C2 cells were seeded in 96-well tissue culture plates at a density of 1×10^4 cells/well and incubated for 12 h. The medium was then replaced with 200 μL of hydrogel extract and incubated for another 24 h and 48 h. Cells cultured in complete medium served as the control. The cell morphology of H9C2 was observed by fluorescence microscopy (ECLIPSE Ts2, Nikon, Japan) after AO staining. Cell viability was investigated using the CCK-8 assay, with absorbance measured at 450 nm using a microplate reader (Infinite M Nano+, Tecan, Austria). Similarly, the cytocompatibility of various concentrations of DFO was also evaluated. The cell viability was calculated using eq 12, where A_{sample} and $A_{control}$ represent the absorbances of CCK-8 solution in hydrogel sample and control group, respectively, A_{blank} represents the absorbance of CCK-8 solution in the absence cell culture.

$$\text{cell viability (\%)} = \frac{A_{sample} - A_{blank}}{A_{control} - A_{blank}} \times 100 \quad (12)$$

4.12. Evaluating the Effects of Hydrogel on Cardiomyocyte Viability under Hypoxia/Reoxygenation Conditions. The hypoxic medium was employed to create the cardiomyocyte hypoxia−reoxygenation (H/R) model according to a previous report.[52] H9C2 cells were seeded in 48-well tissue culture plates at a density of 5×10^4 cells/well and incubated for 12 h. The medium was then removed, and 400 μL of hypoxic medium was added to each well. The cells were incubated in an anoxic chamber with 1% aqueous O_2 and 5% aqueous CO_2 for 2 h. After discarding the hypoxic medium, 60 μL of HS/GMs, HSD/GMs, and HSD/DFO@GMs hydrogel and 500 μL of fresh medium containing 0.5 μg/mL MMP-2 were added, and the cells were incubated for another 12 h under normal condition. Cell viability was determined by CCK-8 assay. Cells that were maintained in the normal incubator throughout the entire incubation period with regular medium changes served as the control group, while cells with the hydrogel replaced by PBS were used as the H/R group.

To evaluate the effect of the prepared HSD/DFO@GMs hydrogel on oxidative stress damage in cardiomyocytes, the cells subjected to

https://doi.org/10.1021/acsami.5c02666
ACS Appl. Mater. Interfaces 2025, 17, 27906−27922

the aforementioned H/R model were stained with dihydroethidium (DHE) and 2′,7′-dichlorofluorescein (DCFH-DA) for 30 min, respectively, followed by staining with 4′,6-diamidino-2-phenylindole (DAPI) for 10 min to investigate the intracellular ROS levels. The lactate dehydrogenase (LDH) level in the cell supernatant was detected by using an LDH kit. Additionally, expression levels of malondialdehyde (MDA) and superoxide dismutase (SOD) in the supernatant of lysed cells were investigated by using the corresponding reagent kit.

To investigate the effects of HSD/DFO@GMs hydrogel on the ferroptosis, H9C2 H/R model cells were stained with Ferro Orange and JC-1 for 20 min at 37 °C for 20 min, respectively, followed by the observation of intracellular Fe^{2+} content and mitochondrial membrane potential using fluorescence microscopy. Additionally, the H/R model cells were incubated with C11- BODIPY for 30 min at 37 °C and then stained with Hoechst 33342 for 5 min to observe the intracellular lipid peroxide content by microscopy. To assess the effect of prepared HSD/DFO@GMs hydrogels on the expression of pro-angiogenic genes, HUVECs were treated with the same method and subjected to immunofluorescence staining for HIF-1α and VEGFA.

4.13. Myocardial Ischemia−Reperfusion Model Construction and Hydrogel Injection. All animal experiments were approved by the Institutional Animal Care and Use Committee of North China University of Science and Technology (Approval SCXK (Beijing) 2020-0004). A myocardial I/R model was established in male Sprague-Dawley (SD) rats (7−8 weeks old, body weight 250 ± 20 g) following previously published protocols.[52] The rats were anesthetized and intubated, and an open thoracotomy was performed at the fourth intercostal space to expose the heart. The left anterior descending (LAD) artery was ligated with a 6−0 suture 2−3 mm distal to the junction between the left auricle and the arterial cone. After ischemia was induced for 30 min, the suture was removed to initiate reperfusion to obtain the myocardial I/R model rats. The I/R rats were randomly assigned into 5 groups: Sham, I/R, HS/GMs, HSD/GMs, and HSD/DFO@GMs. In the Sham group, the rats underwent a thoracotomy without ligation. For the hydrogel-treated group, the hydrogel pre-solution was mixed aseptically using a double pass and 100 μL hydrogels were injected into multiple points in the infarcted area 5 min before removal of the ligature. The wound was then closed with a 3−0 suture to complete the procedure.

4.14. In Vivo ROS Level Measurements. One day after surgery, orbital blood sampling was performed on rats and serum was obtained by centrifugation at 1200 rpm for 20 min after the blood samples had coagulated. LDH, MDA, and SOD kits were used to measure the expression level of the corresponding substances in rat serum. Meanwhile, freshly obtained heart tissues were fixed with OCT and frozen at −80 °C. Cryosections of 4 μm were cut and incubated with DHE, DCFH-DA, and Mito Tracker solution in the dark for 30 min, followed by washing with PBS. DAPI staining was then applied to seal the sections. The sections were examined under a high-speed confocal platform (Andor Dragonfly, Oxford Instruments, U.K.), and the relative fluorescence intensities of DCFH-DA, DHE, and Mito Tracker were analyzed by ImageJ software.

4.15. Immunofluorescence and Histological Staining. At 3 days, 7 days, and 28 days postsurgery, rat hearts were harvested and fixed with 4 wt % paraformaldehyde, dehydrated, paraffin-embedded, and sectioned into 4 μm thick slices. The histological features of the hearts in each group were assessed using Masson (DC0032, Leagene Biotechnology) and H&E staining. The infarct area was quantified by calculating the ratio of fibrotic area (blue) to total area using ImageJ software. Cardiomyocyte ferroptosis was evaluated using antibodies against GPX4 (DF6701, Affinity), ASCL4 (DF12141, Affinity), 4-HNE (HY-P81208, MCE), and Fe^{3+} (G1428, Solarbio). The expression levels of pro-vascular factor levels were evaluated using antibodies against VEGF (A17877, Abcam), HIF-1α (B3301, Biodragon), and α-SMA (904601, Biolegend). TUNEL (AC12L055, LIVE-iLAB) staining was used to evaluate cardiomyocyte apoptosis. Cell membrane staining was performed with WGA (RL1022, VECTOR) staining. cTnT (ET1610-51 HUABIO) staining was selected to investigate the expression level of myocardial-specific proteins. Cell nuclei were stained with DAPI (8961S, Cell Signaling Technology). AF568 antimouse (A10037, Invitrogen) and AF488 antirabbit (A-21026, Invitrogen) were used as the fluorescent secondary antibodies. Images were captured using a high-speed confocal platform (Andor Dragonfly, Oxford Instruments, U.K.) and a fluorescence microscope (BX63, Olympus, Japan). The percentage of apoptosis, expression levels of VEGF, GPX4, ASCL4, and 4-HNE, iron ion content, cardiomyocyte size, and vascular density were analyzed by calculating the fluorescence area and intensity using ImageJ software.

4.16. Echocardiography and Electrocardiogram. On days 1, 7, and 28 postsurgeries, a biosignal processing system (PowerLab System, AD Instruments, Australia) was used to investigate the electrocardiographs (ECGs) of each rat. Briefly, three needle electrodes were inserted subcutaneously into each of the two upper limbs and the right lower limbs. The ECGs of SD rats were recorded at a tracking speed of 50 mm·s^{-1}, and the QRS interval durations were analyzed using LabChart software.

Transthoracic echocardiography was conducted on day 28 postsurgery using a Vevo 3100 LT imaging system (Visual Sonics, Canada). Two-dimensional guided M-mode measurements were taken to obtain a parasternal long-axis view with the cutting plane positioned at the midpoint of the papillary muscle. Measurements of end-systolic diameter (LVDs), end-diastolic diameter (LVDd), ejection fraction (EF), shortening fraction (FS), end-systolic volume (LVSv), and end-diastolic volume (LVDv) were performed to assess the cardiac geometry and function in each group.

4.17. Physiological Toxicity Assay. After 28 days following the implantation of hydrogel into the I/R-injured area, the liver, spleen, lungs,and kidneys of each group of rats were excised and stained with H&E to assess the systemic toxicity of each hydrogel group. Images were captured using a fluorescence microscope (BX63, Olympus, Japan).

4.18. Statistical Analysis. All data were presented as the mean ± standard deviation, derived from at least three independent runs for each sample. Data analysis was performed using Origin 2024b software and Microsoft Excel 2016, employing one-way ANOVA with Tukey's post hoc test. In all cases, a p-value of less than 0.05 was considered statistically significant. n.s. indicates no significant difference at $p > 0.05$.

■ ASSOCIATED CONTENT

Supporting Information

The Supporting Information is available free of charge at https://pubs.acs.org/doi/10.1021/acsami.5c02666.

Morphology and particle size distribution of DFO@GMs; DFO-Fe^{3+} and dopamine standard curves; hydrogel rheological behaviors and injection force; kinetic fitting curves; antioxidant properties; hydrogel−DFO biocompatibilities; AO fluorescence and H&E staining images; protective effects; expression levels; immunofluorescence images; echocardiography parameters; DFO loading in GMs; hydrogel preparation parameters; kinetic adsorption fitting data (PDF)

■ AUTHOR INFORMATION

Corresponding Authors

Hong Sun − *School of Basic Medical Sciences, North China University of Science and Technology, Tangshan 063210, China; Hebei Key Laboratory for Rehabilitation Engineering and Regenerative Medicine, Tangshan 063210, China;* Email: sunhong@ncst.edu.cn

Hong Zhang − *School of Chemical Engineering and Technology, Tianjin University, Tianjin 300350, China; State Key Laboratory of Synthetic Biology (Tianjin*

University), Tianjin 300250, China; orcid.org/0000-0002-6633-9264; Email: zhanghong@tju.edu.cn

Junjie Li − *School of Chemical Engineering and Technology and Frontiers Science Center for Synthetic Biology and Key Laboratory of Systems Bioengineering (Ministry of Education), Tianjin University, Tianjin 300350, China; State Key Laboratory of Synthetic Biology (Tianjin University), Tianjin 300250, China; Hebei Key Laboratory for Rehabilitation Engineering and Regenerative Medicine, Tangshan 063210, China;* orcid.org/0000-0003-2152-6952; Email: li41308@tju.edu.cn

Authors

Jiazhuo Gong − *School of Chemical Engineering and Technology, Tianjin University, Tianjin 300350, China*

Yuwei Qiu − *School of Chemical Engineering and Technology, Tianjin University, Tianjin 300350, China*

Chaojie Yu − *School of Chemical Engineering and Technology, Tianjin University, Tianjin 300350, China*

Cheng Cao − *School of Chemical Engineering and Technology, Tianjin University, Tianjin 300350, China*

Xiuqiang Li − *School of Chemical Engineering and Technology, Tianjin University, Tianjin 300350, China*

Jiajun Lu − *School of Basic Medical Sciences, North China University of Science and Technology, Tangshan 063210, China*

Weiqing Zhao − *School of Basic Medical Sciences, North China University of Science and Technology, Tangshan 063210, China*

Zhongming Zhao − *School of Chemical Engineering and Technology, Tianjin University, Tianjin 300350, China*

Haitao Zhang − *School of Chemical Engineering and Technology, Tianjin University, Tianjin 300350, China*

Fanglian Yao − *School of Chemical Engineering and Technology, Tianjin University, Tianjin 300350, China;* orcid.org/0000-0003-4153-3543

Complete contact information is available at: https://pubs.acs.org/10.1021/acsami.5c02666

Author Contributions

J.G.: Methodology, writing—original draft, and conceptualization. Y.Q.: Methodology and conceptualization. C.Y.: Methodology. C.C.: Data arrangement. X.L.: Conceptualization. J.Lu: Conceptualization. W.Z.: Conceptualization. Z.Z.: Conceptualization. Ha.Zhang: Data arrangement. F.Y.: Funding acquisition and project administration. H.S.: Funding acquisition and project administration. Ho.Zhang: Resources, supervision, and funding acquisition. J.Li: Resources, supervision, funding acquisition, and writing—review and editing.

Notes

The authors declare no competing financial interest.

■ ACKNOWLEDGMENTS

This work was supported by National Natural Science Foundation of China (No. 32471384)

■ REFERENCES

(1) Hashimoto, H.; Olson, E. N.; Bassel-Duby, R. Therapeutic approaches for cardiac regeneration and repair. *Nat. Rev. Cardiol.* **2018**, *15* (10), 585−600.

(2) Heusch, G. Myocardial ischaemia-reperfusion injury and cardioprotection in perspective. *Nat. Rev. Cardiol.* **2020**, *17* (12), 773−789.

(3) Hausenloy, D. J.; Yellon, D. M. Myocardial ischemia-reperfusion injury: a neglected therapeutic target. *J. Clin. Invest.* **2013**, *123* (1), 92−100.

(4) Cai, W. B.; Liu, L.; Shi, X. L.; Liu, Y. A.; Wang, J.; Fang, X.; Chen, Z. P.; Ai, D.; Zhu, Y.; Zhang, X. Alox15/15-HpETE Aggravates Myocardial Ischemia-Reperfusion Injury by Promoting Cardiomyocyte Ferroptosis. *Circulation* **2023**, *147* (19), 1444−1460.

(5) Del Re, D. P.; Amgalan, D.; Linkermann, A.; Liu, Q. H.; Kitsis, R. N. Fundamental Mechanisms of Regulated Cell Death and Implications for Heart Disease. *Physiol. Rev.* **2019**, *99* (4), 1763−1817.

(6) Dixon, S. J.; Lemberg, K. M.; Lamprecht, M. R.; Skouta, R.; Zaitsev, E. M.; Gleason, C. E.; Patel, D. N.; Bauer, A. J.; Cantley, A. M.; Yang, W. S.; Morrison, B.; Stockwell, B. R. Ferroptosis: An Iron-Dependent Form of Nonapoptotic Cell Death. *Cell* **2012**, *149* (5), 1060−1072.

(7) Qin, Y. H.; Qiao, Y.; Wang, D.; Tang, C. C.; Yan, G. L. Ferritinophagy and ferroptosis in cardiovascular disease: Mechanisms and potential applications. *Biomed. Pharmacother.* **2021**, *141*, No. 111872.

(8) Wang, K.; Chen, X. Z.; Wang, Y. H.; Cheng, X. L.; Zhao, Y.; Zhou, L. Y.; Wang, K. Emerging roles of ferroptosis in cardiovascular diseases. *Cell Death Discovery* **2022**, *8* (1), 394.

(9) Wu, X. G.; Li, Y.; Zhang, S. C.; Zhou, X. Ferroptosis as a novel therapeutic target for cardiovascular disease. *Theranostics* **2021**, *11* (7), 3052−3059.

(10) Fang, X. X.; Ardehali, H.; Min, J. X.; Wang, F. D. The molecular and metabolic landscape of iron and ferroptosis in cardiovascular disease. *Nat. Rev. Cardiol.* **2023**, *20* (1), 7−23.

(11) Li, S. H.; Qian, Y. Q.; Zhang, X.; Xu, J. J.; Zhang, R. P. Ferroptosis-inducing nanocomposite hydrogels: A multimodal platform for enhanced cancer therapeutics. *Chem. Eng. J.* **2024**, *500*, No. 157451.

(12) Xu, Q. X.; Xiao, Z. Y.; Yang, Q. Z.; Yu, T. T.; Deng, X. J.; Chen, N. H.; Huang, Y. Y.; Wang, L. H.; Guo, J.; Wang, J. H. Hydrogel-based cardiac repair and regeneration function in the treatment of myocardial infarction. *Mater. Today Bio* **2024**, *25*, No. 100978.

(13) Tang, L. J.; Zhou, Y. J.; Xiong, X. M.; Li, N. S.; Zhang, J. J.; Luo, X. J.; Peng, J. Ubiquitin-specific protease 7 promotes ferroptosis via activation of the p53/TfR1 pathway in the rat hearts after ischemia/reperfusion. *Free Radic. Biol. Med.* **2021**, *162*, 339−352.

(14) Fang, X. X.; Wang, H.; Han, D.; Xie, E. J.; Yang, X.; Wei, J. Y.; Gu, S. S.; Gao, F.; Zhu, N. L.; Yin, X. J.; Cheng, Q.; Zhang, P.; Dai, W.; Chen, J. H.; Yang, F. Q.; Yang, H. T.; Linkermann, A.; Gu, W.; Min, J. X.; Wang, F. D. Ferroptosis as a target for protection against cardiomyopathy. *Proc. Natl. Acad. Sci. U. S. A.* **2019**, *116* (7), 2672−2680.

(15) Ma, X. H.; Liu, J. H. Z.; Liu, C. Y.; Sun, W. Y.; Duan, W. J.; Wang, G.; Kurihara, H.; He, R. R.; Li, Y. F.; Chen, Y.; Shang, H. C. ALOX15-launched PUFA-phospholipids peroxidation increases the susceptibility of ferroptosis in ischemia-induced myocardial damage. *Signal Transduct. Target. Ther.* **2022**, *7* (1), 288.

(16) Hao, T.; Qian, M.; Zhang, Y. T.; Liu, Q.; Midgley, A. C.; Liu, Y. P.; Che, Y. Z.; Hou, J. L.; Zhao, Q. An Injectable Dual-Function Hydrogel Protects Against Myocardial Ischemia/Reperfusion Injury by Modulating ROS/NO Disequilibrium. *Adv. Sci.* **2022**, *9* (15), No. 202105408.

(17) Zhang, C. X.; Cheng, Y.; Liu, D. Z.; Liu, M.; Cui, H.; Zhang, B. L.; Mei, Q. B.; Zhou, S. Y. Mitochondria-targeted cyclosporin A delivery system to treat myocardial ischemia reperfusion injury of rats. *J. Nanobiotechnol.* **2019**, *17*, 18.

(18) Chekini, M.; Krivoshapkina, E.; Shkodenko, L.; Koshel, E.; Shestovskaya, M.; Dukhinova, M.; Kheiri, S.; Khuu, N.; Kumacheva, E. Nanocolloidal Hydrogel with Sensing and Antibacterial Activities Governed by Iron Ion Sequestration. *Chem. Mater.* **2020**, *32* (23), 10066−10075.

(19) Xu, Y. C.; Cai, F.; Zhou, Y. D.; Tang, J. C.; Mao, J. N.; Wang, W.; Li, Z.; Zhou, L.; Feng, Y.; Xi, K.; Gu, Y.; Chen, L. Magnetically

attracting hydrogel reshapes iron metabolism for tissue repair. *Sci. Adv.* **2024**, *10* (33), No. eado7249.
(20) Lyu, Y. N.; Xie, J. H.; Liu, Y.; Xiao, M.; Li, Y.; Yang, J. H.; Yang, J.; Liu, W. G. Injectable Hyaluronic Acid Hydrogel Loaded with Functionalized Human Mesenchymal Stem Cell Aggregates for Repairing Infarcted Myocardium. *ACS Biomater. Sci. Eng.* **2020**, *6* (12), 6926−6937.
(21) Dorsey, S. M.; McGarvey, J. R.; Wang, H.; Nikou, A.; Arama, L.; Koomalsingh, K. J.; Kondo, N.; Gorman, J. H.; Pilla, J. J.; Gorman, R. C.; Wenk, J. F.; Burdick, J. A. MRI evaluation of injectable hyaluronic acid-based hydrogel therapy to limit ventricular remodeling after myocardial infarction. *Biomaterials* **2015**, *69*, 65−75.
(22) Amano, Y.; Qi, P.; Nakagawa, Y.; Kirita, K.; Ohta, S.; Ito, T. Prevention of Peritoneal Adhesions by Ferric Ion-Cross-Linked Hydrogels of Hyaluronic Acid Modified with Iminodiacetic Acids. *ACS Biomater. Sci. Eng.* **2018**, *4* (9), 3405−3412.
(23) Wang, Y.; Zhang, Y.; Yang, Y. P.; Jin, M. Y.; Huang, S.; Zhuang, Z. M.; Zhang, T.; Cao, L. L.; Lin, X. Y.; Chen, J.; Du, Y. Z.; Chen, J.; Tan, W. Q. Versatile dopamine-functionalized hyaluronic acid-recombinant human collagen hydrogel promoting diabetic wound healing via inflammation control and vascularization tissue regeneration. *Bioact. Mater.* **2024**, *35*, 330−345.
(24) Lei, L.; Yuan, J. L.; Yang, Q. Q.; Tu, Q. X.; Yu, H. J.; Chu, L. Z.; Tang, L.; Zhang, C. L. Curcumin-polydopamine nanoparticles alleviate ferroptosis by iron chelation and inhibition of oxidative stress damage. *RSC Adv.* **2024**, *14* (21), 14934−14941.
(25) Feng, Y. S.; Madungwe, N. B.; Aliagan, A. D. I.; Tombo, N.; Bopassa, J. C. Liproxstatin-1 protects the mouse myocardium against ischemia/reperfusion injury by decreasing VDAC1 levels and restoring GPX4 levels. *Biochem. Biophys. Res. Commun.* **2019**, *520* (3), 606−611.
(26) Chen, T. T.; Qin, Y.; Li, Y.; Li, Y. R.; Luo, J. J.; Fan, L. L.; Feng, M. Y.; Wang, Z.; Zhao, Y. J. Chiral Polymer Micelles Alleviate Adriamycin Cardiotoxicity via Iron Chelation and Ferroptosis Inhibition. *Adv. Funct. Mater.* **2023**, *33* (30), No. 2300689.
(27) Tschuck, J.; Nair, V. P. P.; Galhoz, A.; Zaratiegui, C.; Tai, H. M.; Ciceri, G.; Rothenaigner, I.; Tchieu, J.; Stockwell, B. R.; Studer, L.; Cabianca, D. S.; Menden, M. P.; Vincendeau, M.; Hadian, K. Suppression of ferroptosis by vitamin A or radical-trapping antioxidants is essential for neuronal development. *Nat. Commun.* **2024**, *15* (1), 7611.
(28) Gao, M. H.; Monian, P.; Quadri, N.; Ramasamy, R.; Jiang, X. J. Glutaminolysis and Transferrin Regulate Ferroptosis. *Mol. Cell* **2015**, *59* (2), 298−308.
(29) Tu, H.; Zhou, Y. J.; Tang, L. J.; Xiong, X. M.; Zhang, X. J.; Sheikh, M. S. A.; Zhang, J. J.; Luo, X. J.; Yuan, C.; Peng, J. Combination of ponatinib with deferoxamine synergistically mitigates ischemic heart injury via simultaneous prevention of necroptosis and ferroptosis. *Eur. J. Pharmacol.* **2021**, *898*, No. 173999.
(30) Wei, X. J.; Chen, S.; Xie, T.; Chen, H. C.; Jin, X.; Yang, J. M.; Sahar, S.; Huang, H. L.; Zhu, S. J.; Liu, N. B.; Yu, C. J.; Zhu, P.; Wang, W.; Zhang, W. An MMP-degradable and conductive hydrogel to stabilize HIF-1α for recovering cardiac functions. *Theranostics* **2022**, *12* (1), 127−142.
(31) Wang, K.; Yao, S. Y.; Wang, Z. Y.; Shen, L. Y.; Guo, D. S.; Zhu, Y.; Yang, X. Y.; Yu, Q. F.; Gao, C. Y. A Sequential Dual Functional Supramolecular Hydrogel with Promoted Drug Release to Scavenge ROS and Stabilize HIF-1α for Myocardial Infarction Treatment. *Adv. Healthc. Mater.* **2024**, *13* (6), No. 202302940.
(32) Yang, T. N.; Brittenham, G. M.; Dong, W. Q.; Levy, M. N.; Obejero-Paz, C. A.; Kuryshev, Y. A.; Brown, A. M. Deferoxamine prevents cardiac hypertrophy and failure in the gerbil model of iron-induced cardiomyopathy. *J. Lab. Clin. Med.* **2003**, *142* (5), 332−340.
(33) Feng, W. Y.; Xiao, Y. J.; Zhao, C. A. F.; Zhang, Z. M.; Liu, W.; Ma, J.; Ganz, O. M.; Zhang, J. L.; Liu, S. J. New Deferric Amine Compounds Efficiently Chelate Excess Iron to Treat Iron Overload Disorders and to Prevent Ferroptosis. *Adv. Sci.* **2022**, *9* (29), No. 202202679.
(34) Saito, T.; Tabata, Y. Hypoxia-induced angiogenesis is increased by the controlled release of deferoxiamine from gelatin hydrogels. *Acta Biomater.* **2014**, *10* (8), 3641−3649.
(35) Wang, Y.; Liu, Z.; Lin, T. M.; Chanana, S.; Xiong, M. P. Nanogel-DFO conjugates as a model to investigate pharmacokinetics, biodistribution, and iron chelation in vivo. *Int. J. Pharm.* **2018**, *538* (1−2), 79−86.
(36) Hamilton, J. L.; Ul-Haq, M. I.; Abbina, S.; Kalathottukaren, M. T.; Lai, B. F. L.; Hatef, A.; Unniappan, S.; Kizhakkedathu, J. N. In vivo efficacy, toxicity and biodistribution of ultra-long circulating desferrioxamine based polymeric iron chelator. *Biomaterials* **2016**, *102*, 58−71.
(37) Lazaridou, M.; Christodoulou, E.; Nerantzaki, M.; Kostoglou, M.; Lambropoulou, D. A.; Katsarou, A.; Pantopoulos, K.; Bikiaris, D. N. Formulation and In-Vitro Characterization of Chitosan-Nanoparticles Loaded with the Iron Chelator Deferoxamine Mesylate (DFO). *Pharmaceutics* **2020**, *12* (3), 238.
(38) Zhang, X. P.; Sun, Y. G.; Yang, R.; Liu, B.; Liu, Y.; Yang, J. H.; Liu, W. G. An injectable mitochondria-targeted nanodrug loaded-hydrogel for restoring mitochondrial function and hierarchically attenuating oxidative stress to reduce myocardial ischemia-reperfusion injury. *Biomaterials* **2022**, *287*, No. 121656.
(39) Liao, X.; Song, X. D.; Li, J. J.; Li, L. S.; Fan, X. L.; Qin, Q.; Zhong, C. B.; Yang, P. Z.; Zhan, J.; Cai, Y. B. An injectable co-assembled hydrogel blocks reactive oxygen species and inflammation cycle resisting myocardial ischemia-reperfusion. *Acta Biomater.* **2022**, *149*, 82−95.
(40) Fan, C. X.; Shi, J. J.; Zhuang, Y.; Zhang, L. L.; Huang, L.; Yang, W.; Chen, B.; Chen, Y. Y.; Xiao, Z. F.; Shen, H.; Zhao, Y. N.; Dai, J. W. Myocardial-Infarction-Responsive Smart Hydrogels Targeting Matrix Metalloproteinase for On-Demand Growth Factor Delivery. *Adv. Mater.* **2019**, *31* (40), No. 1902900.
(41) Yang, F.; Guo, G. Y.; Wang, Y. B. Inflammation-triggered dual release of nitroxide radical and growth factor from heparin mimicking hydrogel-tissue composite as cardiovascular implants for anti-coagulation, endothelialization, anti-inflammation, and anti-calcification. *Biomaterials* **2022**, *289*, No. 121761.
(42) Yu, C. J.; Yue, Z. W.; Zhang, H.; Shi, M. Y.; Yao, M. M.; Yu, Q. Y.; Liu, M.; Guo, B. Y.; Zhang, H. T.; Tian, L. Q.; Sun, H.; Yao, F. L.; Li, J. J. Ultra-Histocompatible and Electrophysiological-Adapted PEDOT-Based Hydrogels Designed for Cardiac Repair. *Adv. Funct. Mater.* **2023**, *33* (15), No. 2211023.
(43) Qiu, Y. W.; Yu, C. J.; Yue, Z. W.; Ren, Y. C.; Wang, W. T.; Yu, Q. Y.; Guo, B. Y.; Liang, L.; Yao, F. L.; Zhang, H.; Sun, H.; Li, J. J. Chronological-Programmed Black Phosphorus Hydrogel for Responsive Modulation of the Pathological Microenvironment in Myocardial Infarction. *ACS Appl. Mater. Interfaces* **2024**, *16* (14), 17323−17338.
(44) Lu, H. Y.; Xiao, H.; Dai, M. Y.; Xue, Y. C.; Zhao, R. Britanin relieves ferroptosis-mediated myocardial ischaemia/reperfusion damage by upregulating GPX4 through activation of AMPK/GSK3β/Nrf2 signalling. *Pharm. Biol.* **2022**, *60* (1), 38−45.
(45) Ding, X. Y.; Xing, X. W.; Liu, J. F.; Zhu, P. C.; Wang, C.; Bai, R.; Kong, B.; Zeng, C. Y.; Zhang, W.; Yue, Y.; Zhang, H. T.; Xiang, J. J.; Yuan, Z. Q.; Liu, Z. Q. Cobweb-Inspired Microenvironment-Targeting Nanosystem with Sequential Multiple-Stage Stimulus-Response Capacity for Ischaemic Tissue Repair. *Adv. Funct. Mater.* **2023**, *33* (32), No. 2301451.
(46) Ifkovits, J. L.; Tous, E.; Minakawa, M.; Morita, M.; Robb, J. D.; Koomalsingh, K. J.; Gorman, J. H.; Gorman, R. C.; Burdick, J. A. Injectable hydrogel properties influence infarct expansion and extent of postinfarction left ventricular remodeling in an ovine model. *Proc. Natl. Acad. Sci. U. S. A.* **2010**, *107* (25), 11507−11512.
(47) Yu, C. J.; Yue, Z. W.; Shi, M. Y.; Jiang, L. J.; Chen, S.; Yao, M. M.; Yu, Q. Y.; Wu, X. J.; Zhang, H.; Yao, F. L.; Wang, C. Y.; Sun, H.; Li, J. J. An Intrapericardial Injectable Hydrogel Patch for Mechanical-Electrical Coupling with Infarcted Myocardium. *ACS Nano* **2022**, *16* (10), 16234−16248.
(48) Shao, Z. J.; Yin, T. Y.; Jiang, J. B.; He, Y.; Xiang, T.; Zhou, S. B. Wound microenvironment self-adaptive hydrogel with efficient

angiogenesis for promoting diabetic wound healing. *Bioact. Mater.* **2023**, *20*, 561−573.
(49) Zhang, Y. B.; Ren, X. Y.; Wang, Y.; Chen, D. X.; Jiang, L.; Li, X.; Li, T.; Huo, M. F.; Li, Q. Targeting Ferroptosis by Polydopamine Nanoparticles Protects Heart against Ischemia/Reperfusion Injury. *ACS Appl. Mater. Interfaces* **2021**, *13* (45), 53671−53682.
(50) Li, J. J.; Guo, S. Z.; Wang, M.; Ye, L.; Yao, F. L. Poly(lactic acid)/poly(ethylene glycol) block copolymer based shell or core cross-linked micelles for controlled release of hydrophobic drug. *RSC Adv.* **2015**, *5* (25), 19484−19492.
(51) Hua, R.; Li, Z. K. Sulfhydryl functionalized hydrogel with magnetism: Synthesis, characterization, and adsorption behavior study for heavy metal removal. *Chem. Eng. J.* **2014**, *249*, 189−200.
(52) Qian, W. Q.; Liu, D. Z.; Han, Y.; Liu, M.; Liu, B.; Ji, Q. F.; Zhang, B. L.; Mei, Q. B.; Zhou, S. Y.; Cheng, Y. Cyclosporine A-loaded apoferritin alleviates myocardial ischemia-reperfusion injury by simultaneously blocking ferroptosis and apoptosis of cardiomyocytes. *Acta Biomater.* **2023**, *160*, 265−280.

https://doi.org/10.1021/acsami.5c02666
ACS Appl. Mater. Interfaces 2025, 17, 27906−27922